Mechanochromic optical/electrical skin for ultrasensitive dual-signal sensing

Heng Zhang[1], Haomin Chen[1], Jeng-Hun Lee[1], Eunyoung Kim[1], Kit-Ying Chan[1,2], Harun Venkatesan[1], Xi Shen[1,2]*, Jinglei Yang[1,3]*, and Jang-Kyo Kim[1,4]*

H. Zhang, Dr H. Chen, Dr J.H. Lee, E. Kim, Dr K.Y. Chan, Dr H. Venkatesan, Prof. X. Shen, Prof. J. Yang, Prof. J.K. Kim
[1] Department of Mechanical and Aerospace Engineering, The Hong Kong University of Science and Technology, Clear Water Bay, Kowloon, Hong Kong 999077, China.
[2] Department of Aeronautical and Aviation Engineering, The Hong Kong Polytechnic University, Hung Hom, Kowloon, Hong Kong 999077, China.
[3] HKUST Shenzhen-Hong Kong Collaborative Innovation Research Institute, Futian, Shenzhen 518048, China.
[4] School of Mechanical and Manufacturing Engineering, The University of New South Wales, Sydney, NSW 2052, Australia.
E-mail: xi.shen@polyu.edu.hk (X. Shen); maeyang@ust.hk (J. Yang); mejkkim@ust.hk (J.K. Kim)

Keywords: interactive sensing, structural color, mechanochromism, stretchable electronics, dual-signal.

Following earlier research efforts dedicated to the realization of multifunctional sensing, recent developments of artificial skins endeavour to go beyond human sensory functions by integrating interactive visualization of strain and pressure stimuli. Inspired by the microcracked structure of spider-slit-organs and mechanochromic mechanism of chameleons, this work aims to design a flexible optical/electrical skin (OE-skin) capable of responding to complex stimuli with interactive feedback of human-readable structural colors. The OE-skin consists of an ionic electrode combined with an elastomer dielectric layer, a chromotropic layer containing photonic crystals and a conductive carbon nanotube/MXene layer. The electrode/dielectric layers function as a capacitive pressure sensor. The mechanochromic photonic crystals of ferroferric oxide-carbon magnetic arrays embedded in the gelatin/polyacrylamide stretchable hydrogel film perceive strain and pressure stimuli with bright color switching outputs in the full visible spectrum. The underlying microcracked conductive layer is devoted to ultrasensitive strain sensing with a gauge factor of 191.8. The multilayered OE-skin delivers an ultrafast, accurate response for capacitive pressure sensing with a detection limit of 75 Pa and long-term stability of 5000 cycles, while visualizing

complex deformations in the form of high-resolution spatial colors. These findings offer new insights into the rational design of OE-skins as multifunctional sensing devices.

1. Introduction

The increasingly versatile requirements of wearable devices have motivated researchers to develop artificial electronic skins (E-skins) as state-of-the-art tactile sensors in the areas of human-machine interfaces,[1, 2] artificial intelligence,[3-6] Internet of Things,[7] and soft robotics.[8-10] E-skins are explored to effectively mimic human somatosensory functions so as to perceive and encode external physical and mechanical stimuli, such as static and dynamic pressures, touch, tension and vibration, into detectable signals like resistance, capacitance, current, and voltage.[11-14] Considerable efforts have been directed towards empowering the sensors with multifunctional sensing capabilities and tissue-like deformability of human skin, while incorporating required functional characteristics, such as high sensitivities, low detection limits and superior spatial acuity.[15, 16]

More recently, studies on e-skins progressed beyond mimicking human skin to develop more fascinating features, such as strain and pressure visualization.[10, 17-22] To enable direct, intelligent interaction between devices and users, various interactive e-skins have been designed to transduce spatially resolved sensing data into the most straightforward readout, i.e., visual signals.[23-30] For example, light-emitting devices and luminescent materials were employed to visualize external stimuli with intensity changes where the electronic sensors have a dual-signal capability to yield accurate electrical responses and instantaneous visual readouts.[22, 25, 31-34] However, the brightness is susceptible to ambient light and human eyes are insensitive to luminance variations, making it difficult to perceive errorless visual information. Chromotropic elements with a wide color-switching range are in high demand for sensitive dual-signal sensing due to their high-contrast visual interaction and easier color spectrum detection.[32, 35-37] Recently, we also designed photonic crystals of magnetic

nanoparticle arrays that exhibited bright color switching in response to in-plane strain stimuli in the full visible spectrum.[38] Based on the structural color mechanism,[33, 38-44] the dimensional changes induced by external forces to sensing components led to alteration of nanocrystal lattices, which allowed the structural color pattern to precisely reflect the spatial distribution of stress/strain.[45-47] With this high-resolution stress distribution, the dual-signal mode e-skin was able to provide valuable quantitative information for visualizing complex deformations and resolving tactile forces.[34, 48-50]

Apart from structural color elements, different conductive agents, such as carbon nanotubes (CNTs), ionic liquids and electrolyte salts, are often integrated into the flexible hydrogel matrix of chromotropic sensors to identify external strains or pressures in the form of electrical resistance and capacitance signals.[51] However, most current dual-signal e-skins suffer from low sensitivities of electrical signals because of inherent limitations of the electromechanical properties of conductive fillers and ion conduction.[36, 42, 48-50, 52-54] To address this challenge, we proposed microcracked structures to enable ultrasensitive strain sensing with a low detection limit, a fast response time and long-term durability based on the crack opening/closure phenomenon.[5, 31, 55] Microcracks that are formed and propagated uniformly across the whole sensor with increasing applied strain could promote the increase in resistance, resulting in an ultrahigh strain sensitivity with a high gauge factor (GF).[5] Introduction of crack propagation mechanism would enable dual-signal e-skins with more accurate and reliable electrical signals in practical applications. Thus, the development of dual-signal sensors with functional features like ultrahigh sensitivity and wide color-switching range is highly desirable for multifunctional sensing with high-level user interaction.[52-54, 56]

Motivated by the mechanochromic mechanism of chameleons and microcracked structure of spider-slit-organs, we developed an ultrasensitive dual-signal optical/electrical e-skin (OE-skin). Multilayer sensors consisting of a PAM hydrogel electrode layer, a polydimethylsiloxane (PDMS) dielectric layer, a gelatin/polyacrylamide (PAM) film

containing Fe_3O_4@C photonic crystal arrays and a microcracked CNT/MXene hybrid conductive layer were integrated into an OE skin, as shown in Figure 1. It served as a multifunctional sensor capable of visualizing external strains and pressures via bright color-switching in the full visible spectrum at a high, reversible spatial resolution thanks to the mechanochromic Fe_3O_4@C crystals. A special emphasis was placed on controlling the magnetic particles size and sample-magnet distance to obtain a series of films with a wide range of structural colors. The crack propagation mechanism of the CNT/MXene conductive layer endowed the OE-skin with an ultrahigh strain sensitivity of GF = 191.8 and a fast response time of 43 ms. The strain sensing performance of the current chromotropic OE-skin is among the best, especially in terms of the range of reflectance wavelength and strain sensitivity, when compared with the existing state-of-the-art sensors. This novel OE-skin may offer new insights into the development of human-machine interactive electronic devices in the future.

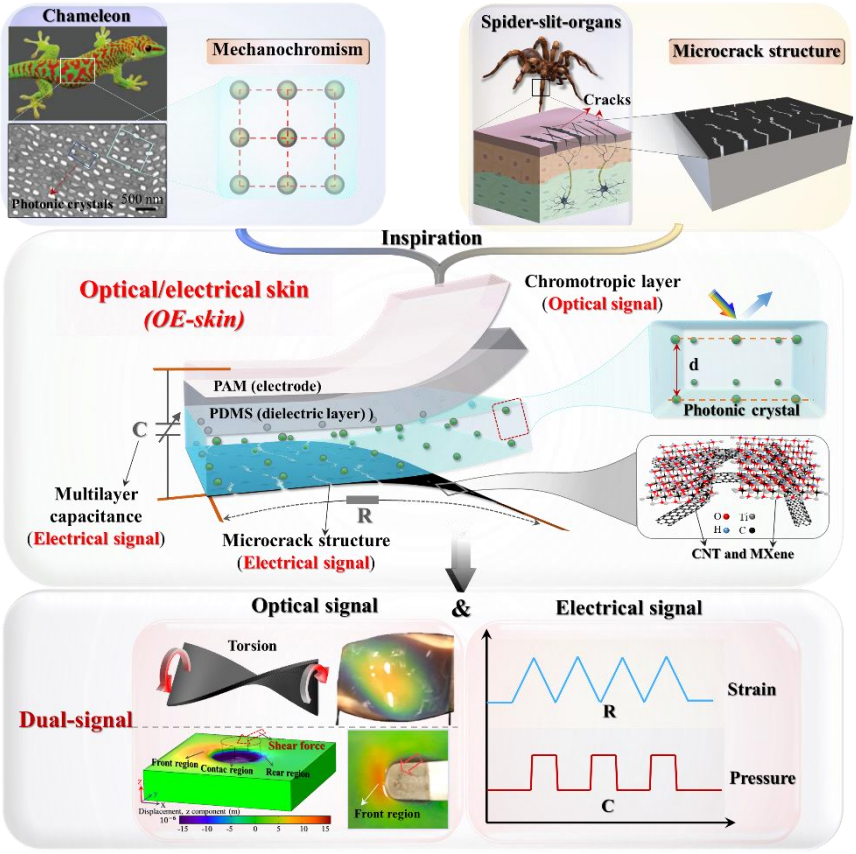

Figure 1. Schematic illustration of the bioinspired mechanochromic OE-skin.

2. Results and Discussion

2.1 Synthesis and characterization of OE-skin

The design concept and fabrication processes of OE-skin is shown in Figure 2a. The magnetic Fe_3O_4@C nanoparticles were synthesized by a hydrothermal process of ferrocene precursor.[57] They had a spherical shape and a uniform size (Figure 2b) with a core/shell structure (Figure 2c and Figure S1a). The outer carbon shell encapsulates the inner clusters consisting of many primary magnetite crystallites with an interplanar spacing of 0.284 nm between the (220) planes (Figure S1b). These ferrimagnetic nanoparticles with superparamagnetic nature had a magnetization value of 25.3 emu/g under a 1 kOe magnetic field, as illustrated by the magnetization curve retaining a sigmoidal shape without a hysteresis loop (Figure S2). Subsequently, gelatin possessing abundant functional groups, such as amino acids, -NH_2 and -OH groups (Figure 2d) was employed to assist the dispersion and stabilization of magnetic particles in solvents. PAM was selected as the secondary hydrogel constituent to form an interpenetrating network structure utilizing its excellent flexibility, durability and biocompatibility.[49] After dispersion of Fe_3O_4@C nanoparticles in the mixture of gelatin/PAM monomers and a chemical crosslinking agent, a highly-ordered photonic crystal array was formed under the balance of interparticle electrostatic repulsion force and magnetic attraction force coming from the external magnetic field. When the precursor was frozen, the physically crosslinked gelatin networks were formed through the hydrogen bond interaction. Thereafter, under UV light with a wavelength of 365 nm at 4 ℃, the randomly distributed PAM monomers were chemically crosslinked with the active functional groups of gelatin chains to form dual-crosslinked hydrogel networks.

High transmittance is also crucial for designing chromotropic OE-skins so that the reflected structural color would not be affected and obscured. High transparency up to 100% in the visible range is preferred when adhering to the PDMS dielectric and PAM ionic electrode layers on top of the chromotropic layer. As shown in the transmission spectra of PAM and

PDMS (Figure 2e), the transparency of inherently yellow gelatin increased to 85% after forming a gelatin/PAM assembly, making it favorable for transmittance of structural color. Additionally, the Fe_3O_4@C magnetic particles embedded in the gelatin/PAM matrix had a sufficiently large center-to-center distance, revealing non-close-packed arrangement as shown in the cross-sectional scanning electron microscopy (SEM) image of the chromotropic film (Figure 2f). These photonic crystals were 530 and 610 nm apart in two orthogonal directions, as shown by the transmission electron microscope (TEM) image and the corresponding Fe and O elemental maps (Figure 2g-i).

The conductive CNT/MXene layer was prepared by mixing the separately dispersed CNTs and MXene nanosheets, as shown in Figure S3. Specifically, the MXene nanosheets were prepared by selective etching of MAX phase precursor (Ti_3AlC_2) in an acidic solution. The loosely stacked accordion-like multilayer structure in Figure 2j indicates that Ti_3AlC_2 was successfully etched into ultrathin MXene nanosheets of 1.8 nm in thickness (in inset) and ~3.6 μm in lateral size (Figure S4). The main elements of MXene, namely Ti, C, O and F, were characterized by X-ray photoelectron spectroscopy (XPS) (Figure S5). The conductive films with uniformly distributed CNTs and MXene sheets (Figure 2k) were obtained after vigorous stirring and vacuum filtration of the mixture of CNT and MXene dispersion. The film was attached to the back of the Fe_3O_4@C/gelatin/PAM layer to function as strain sensor while its dark color effectively prevented the background color from interfering with the structural color of the chromotropic layer. Microcracks were formed in the brittle CNT/MXene thin film when the flexible chromotropic film was stretched. These microcracks (Figure 2l) were widened and closed (Figure 2m) upon repeated stretching and releasing, respectively, which in turn enabled a drastic change in resistance and thus an ultrahigh strain sensitivity. The top capacitive film comprising the PAM electrode layer and the PDMS dielectric layer (Figure S6) served as the pressure sensor. Finally, the integrated e-skin assembly was encapsulated with a thin layer of PDMS to avoid water evaporation so as to ensure its long-term operation and

durability (Figure S7).

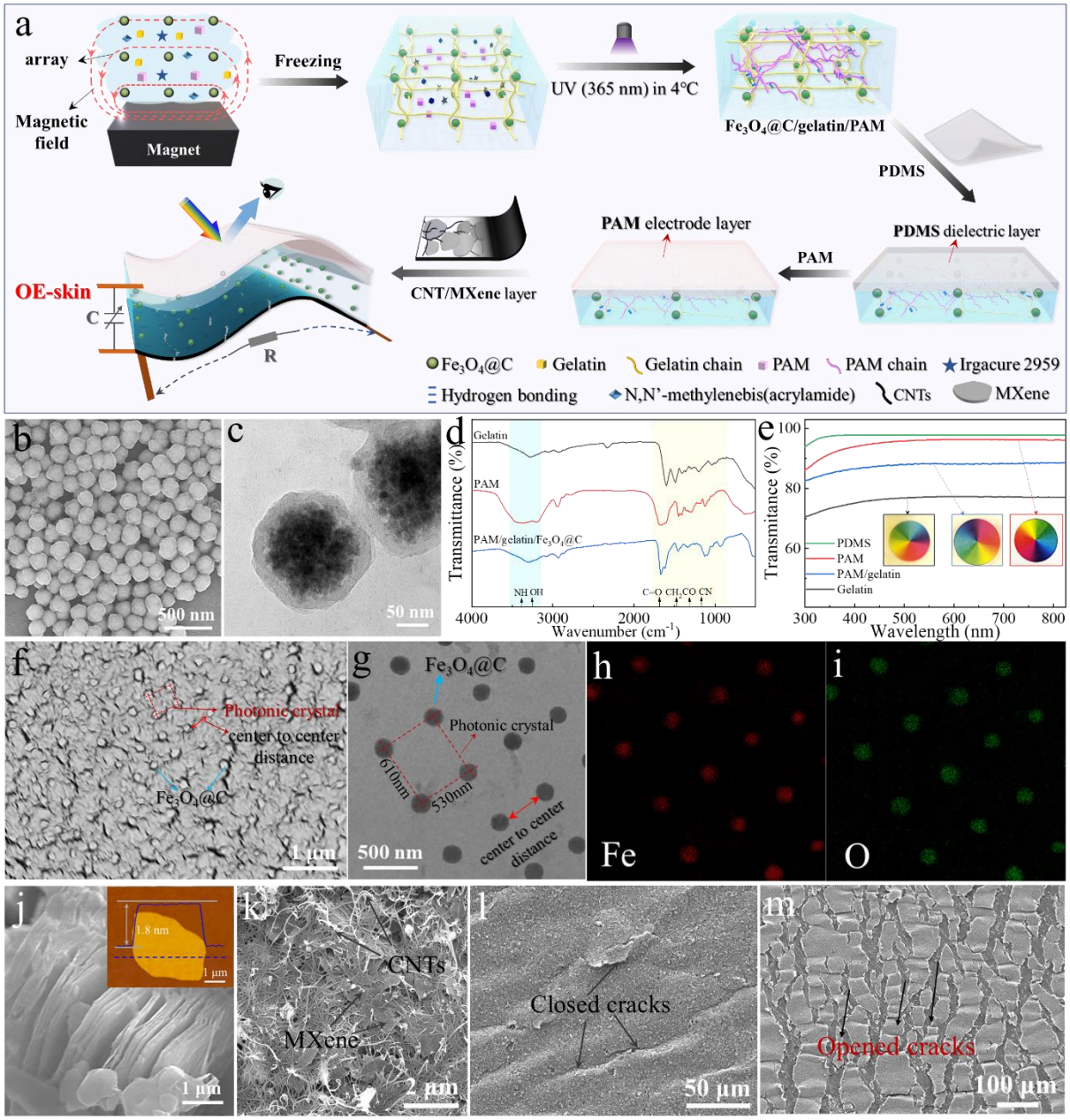

Figure 2. Structural design of OE-skin. (a) Fabrication process of the multilayered chromotropic OE-skin. (b) SEM image of Fe_3O_4@C magnetic nanoparticles with a uniform size. (c) High resolution TEM image of core-shell structure of Fe_3O_4@C nanoparticles. (d) Fourier transform-infrared (FT-IR) spectra of gelatin, PAM and Fe_3O_4@C/gelatin/PAM hydrogels. (e) UV-vis spectra of gelatin, PAM, gelatin/PAM and PDMS thin films with photographs of hydrogels on a color code in inset. (f) SEM image of the Fe_3O_4@C particle array embedded in the gelatin/PAM matrix. (g) TEM image of the Fe_3O_4@C photonic crystals

and corresponding (h) Fe and (i) O elemental maps. (j) SEM image of exfoliated MXene and atomic force microscope (AFM) image of a 1.8 nm thick MXene nanosheet in inset. SEM images of the CNT/MXene film (k) before crack opening, and with (l) closed and (m) opened microcracks.

2.2 Material and structural optimization

The material and structural properties of each layer are key parameters influencing the optical, mechanical and electrical performance of the OE-skin. According to the Bragg's law, the initially reflected structural colors of the chromotropic film are dependent on the center-to-center distance between the adjacent nanoparticles of the non-close-packed Fe_3O_4@C photonic crystal array, which could be altered by the size of magnetic nanoparticles and the strength of external magnetic field. The diameters of Fe_3O_4@C magnetic nanoparticles were varied from 130 to 250 nm by controlling the amount of H_2O_2 in the hydrothermal synthesis process, as summarized in Figure 3a. After immobilizing these nanoparticles in the gelatin/PAM matrix under an external magnetic field, the corresponding reflectance spectra of the film containing particles of different diameters covered the full visible spectrum ranging from violet (435 nm) to dark color (680 nm), as shown in Figure 3b. The coverage of wide spectrum enabled us to choose any initial color depending on the application. It should be noted that the concentration of Fe_3O_4@C in the gelatin/PAM hydrogel did not affect the color of the chromotropic film but the color intensity (Figure S8), so that a high concentration of 40 mg/ml was chosen for the film preparation in this work to obtain deep and bright visual colors. Apart from hydrogel concentration, the magnetic field strength which was regulated by adjusting the distance between the magnet and the pregel solution was also a key parameter determining the visual color. A longer sample-magnet distance meant a red-shifted reflection peak of the Fe_3O_4@C/gelatin/PAM solution due to the longer interparticle distance of photonic crystals under a lower magnetic strength (Figure S9). The visual color of the pregel solution did not change even after polymerization via crosslinking, as shown in Figure S10.

Thus, by controlling the magnetic particles size and sample-magnet distance, we were able to obtain a series of films with a wide range of structural colors (Figure 3c).

To optimize the mechanical properties of the photonic crystal matrix, such as stretchability, tensile and compression strengths, recyclability and adhesion, the gelatin to PAM weight ratio was controlled, as shown in Figure 3d-3g. Benefiting from double synergistic networks, the gelatin/PAM hydrogels exhibited much higher deformation than the pure gelatin. When the gelatin concentration was increased from 5 to 15 wt%, both the tensile strength and ductility of the matrix enhanced with its elastic modulus surging from 8.95 to 35.4 kPa and the fracture strain from 150 to 810%. A similar mechanical property enhancement was also observed with increasing gelatin concentration due to the formation of more dynamic noncovalent and hydrogen bonds between the active functional groups of gelatin and PAM chains. Apart from the tensile properties, the compressive modulus increased to 38.8 kPa as the gelatin/PAM concentration was raised to 10%/10% (Figure 3e). The hydrogel well sustained 400 cycles of compression/release of 70% strain, as shown in Figure 3f. A clear hysteresis loop was found in the first cycle because of the extensive energy dissipation from the damage of weak internal networks. In the subsequent cycles, the dissipated energy remained almost constant due to the stabilized network structure, demonstrating superior recoverability and stability. A high gelation concentration of 10 wt% or more in the gelatin/PAM hydrogel facilitated excellent adhesion strength owing to the abundant functional groups in the gelatin chains, as shown in Figure 3g and Figure S11. The strong adhesion of the hydrogel with different materials (Figure S12), such as glass, metal and PDMS, ensured sufficient bonding of the Fe_3O_4@C/gelatin/PAM chromotropic layer with the surrounding PDMS dielectric layer and conductive CNT/MXene layer required for assembling the multilayered OE-skin. In view of the satisfactory stretchability and adhesion strength of the gelatin/PAM hydrogel, a weight ratio of 10%/10% was chosen for further study.

The in-plain strain sensing performance of the e-skin was enhanced by optimizing the

electrical properties of the CNT/MXene layer. The conductive layer had an extremely low initial resistance, R_0, because of its high electrical conductivity of ~ 920 S/cm (Figure S13) and therefore the increment in its relative resistance normalized by the initial resistance, $\frac{\Delta R}{R_0}$, with increasing strain was significant. As such, the OE-skin containing a conductive layer showed a functionally similar, yet much larger increase in $\frac{\Delta R}{R_0}$ against applied strain, ε, than the sample without one (Figure 3h-i). The sensitivity of the OE-skin for strain sensing was measured by the gauge factor (GF = $(\frac{\Delta R}{R_0})/\varepsilon$). The introduction of 2D MXene nanosheets into the CNT film ameliorated the strain sensing performance with higher sensitivities as the MXene content increased. As shown in Figure 3j and S14, the GF value surged to 191.8 when the concentration of MXene increased to 50 wt% before it became saturated at higher MXene contents. In view of potential reductions of ductility of the film with the addition of MXene nanosheets, we have chosen 50 wt% MXene for further study. It is also interesting to note that the film thickness of up to about 15 μm had a positive effect on GF, as shown in Figure 3k and S15. The thicker the film was, the larger the fragments of conductive layer were and thus the greater the crack width running among them at a given strain (Figure S16). The larger gaps between the conducting fragments in the thicker films mean difficulties in electron tunneling with an associated higher resistance. To satisfy the requirement of wearable nature of OE-skins, an optimal film thickness of 15 μm was selected.

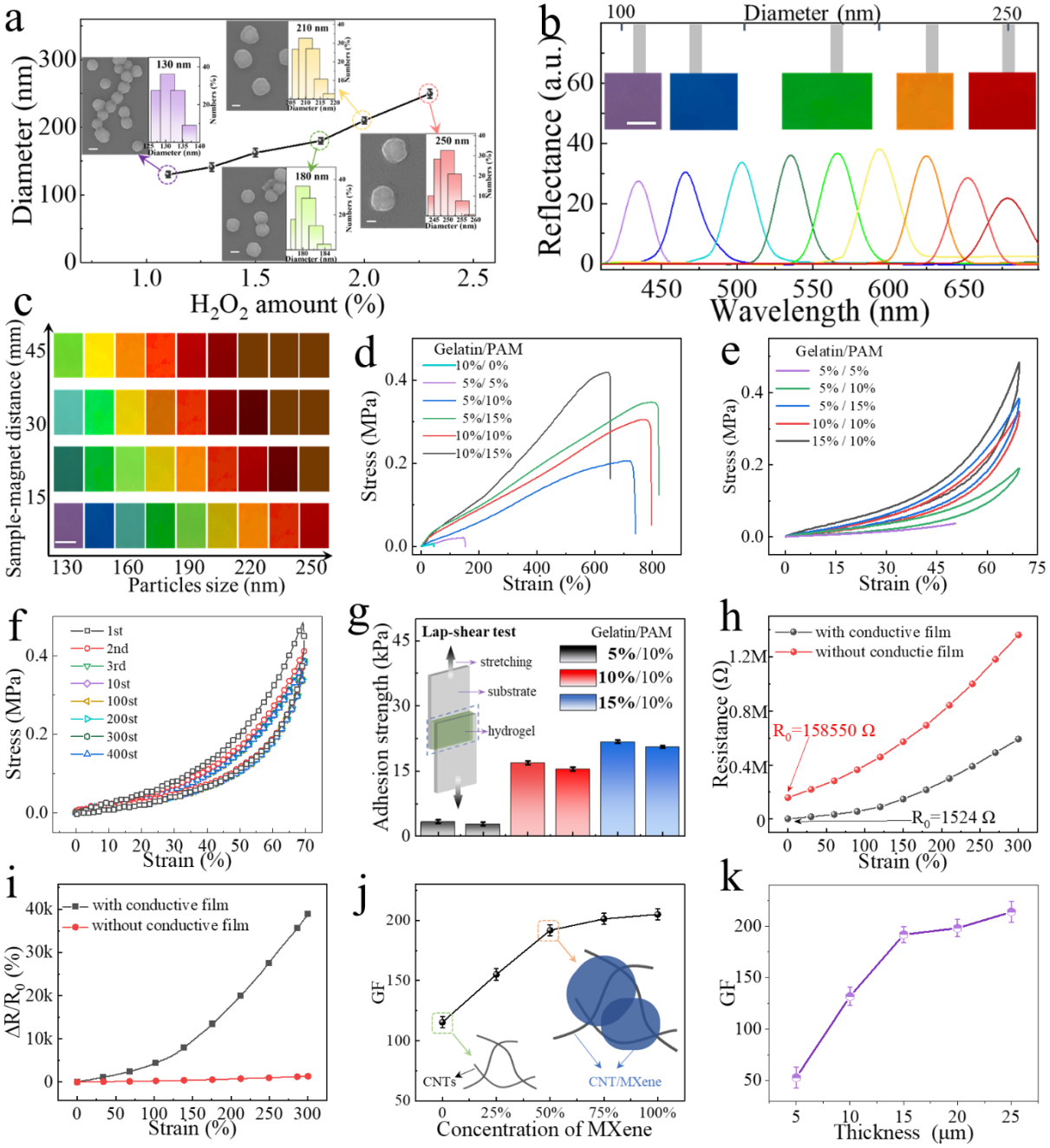

Figure 3. Tunable optical, mechanical and electrical properties. (a) Relationship between the diameter of magnetic nanoparticles and the amount of added H_2O_2. The insets are SEM images and diameters of corresponding nanoparticles. (b) Optical structural colors and corresponding reflectance spectra of the chromotropic films containing nanoparticles with different diameters. Scale bar = 1 cm. (c) A series of chromotropic films with structural colors ranging from violet to dark red for different nanoparticle sizes and sample-magnet distances. Scale bar = 1 cm. (d) Tensile stress-strain curves and (e) Compressive stress-strain curves of

the chromotropic films prepared with different gelatin/PAM weight ratios. (f) Loading-unloading cycles of the gelatin/PAM (10%/10%) hydrogel to maximum 70% compressive strain. (g) Adhesion strength of the gelatin/PAM hydrogels with glass and PDMS substrates for different weight ratios. (h) Comparison of initial resistance, R_0, and resistance change under stretching of OE-skins with and without conductive films. (i) Comparison of relative resistance variation under different strains for OE-skins with and without conductive films. (j) GF of OE-skins as a function of MXene concentration in the conductive film. (k) GF of OE-skins prepared with CNT/MXene films of different thicknesses.

2.3 Optical/electrical response to in-plane stretching and compression

The optimized chromotropic OE-skin shows excellent optical and electrical sensing performance by virtue of the mechaochromism of Fe_3O_4@C photonic crystals and unique microcracked conductive layer. The structurally colored OE-skin underwent a gradual color-switching from initially dark red to violet upon stretching from 0 to 230% strain, as shown in Figure 4a. During uniaxial tension, the reflectance wavelength continuously blue-shifted from 680 to 430 nm (Figure 4b). This color-switching phenomenon can be explained using a schematic diagram (Figure 4c), which is modeled by the following equation:[37, 52]

$$\lambda_{max} = 2d(1 - \nu\varepsilon_x)n_{eff} \quad (1)$$

where λ_{max} is reflectance wavelength corresponding to the peak position, d is the center-to-center distance between adjacent particles in photonic structures, n_{eff} is the effective refractive index of gelatin/PAM matrix, ε_x is tensile strain applied along the longitudinal direction, and ν is the Poisson's ratio. Upon stretching, the thickness of matrix through the observation direction (z) was reduced due to Poisson effect while the center-to-center distance of particles subsequently decreased from d_0 to d_1, resulting in a reduced λ. Upon releasing tensile strain, the film rapidly returned to its original state, accompanied by a full recovery of reflected visual colors. A highly linear relationship between λ_{max} and ε_x over the entire

sensing range (0-230%) is displayed in Figure 4d. The mechanochromic sensitivity for strain sensing, which is defined as the $\Delta\lambda/\Delta\varepsilon$,[49] was calculated to be ~1.06 nm%$^{-1}$. Conversely, when the material is compressed in the longitudinal direction, λ_{max} increased due to the enlarged thickness and center-to-center distance, prompting a red-shift color switching from green to dark red, as shown in Figure S17. It follows that accurate in-plane tensile or compressive stress states can be identified in a mechanochromic film according to the foregoing color-switching mechanism.

Apart from visual optical signals enabled by the chromotropic layer, electromechanical properties of the optimized OE-skin with a CNT/MXene weight ratio of 1:1 and a thickness of 15 μm were characterized by recording the typical $\Delta R/R_0$-strain curve, as shown in Figure 4d. This curve exhibited different strain sensitivities in two distinct stages: namely, GF of 47.2 at low strains from 0 to 130% and GF of 191.8 at high strains from 130 to 300%. A highly sensitive strain sensing capability is related to the strain-dependent crack propagation mechanism, as schematically illustrated in Figure 4e. There were two independent conducting networks acting on the OE-skin when a tensile strain was applied, namely the CNT/MXene conductive layer with a low resistance and the gelatin/PAM hydrogel layer with a high resistance (Figure 3h). However, the destruction of conductive networks leading to an increase in resistance in tension arose mainly from the formation of cracks in the conductive layer, whereas the conduction by electron transfer in the hydrogel layer remained largely unchanged, especially at high strains above 50% (Figure S18). The SEM images in Figure 4f present the changes in morphologies of the conductive layer when the strain was gradually increased to 300%. At low strains, the reduced number of contact points between neighboring 2D MXene flakes played a dominant role in hindering the electron transfer due to the increase in crack width whereas the 1D CNTs still bridging the microcracks. As the strain increased, fragments became increasingly smaller through the generation of more cracks, while bridged CNTs remained intact and the crack width did not grow much. When the applied strain was

very high, say beyond 130%, only the CNT network connected isolated fragments for electron transfer, giving rise to a high resistance and thus an ultrahigh GF. The exceptionally high GF of the E-skin was accompanied by a fast response/recovery time of 43 ms (Figure 4g) and stable resistance changes under different stretching frequencies (Figure S19). The high stability of strain response was confirmed by the consistent resistances measured when the OE-skin was subjected to cycles at different strains ranging from an extremely low detection limit of 0.1% to a maximum of 300% (Figure 4h). More interestingly, both the optically reflected wavelength and electrical resistance variations maintained highly consistent (Figure 4i) for over 3000 stretching/releasing cycles in the long-term durability test, verifying the potential of practical applications. These foregoing results signify that our chromotropic OE-skin possessed excellent optical and electrical dual-signal responses to tensile strain stimuli. Indeed, its strain sensing performance is among the best, especially regarding the range of reflectance wavelength and strain sensitivity, when compared with existing state-of-the-art sensors reported in the literature (Figure S20 and Table S1).

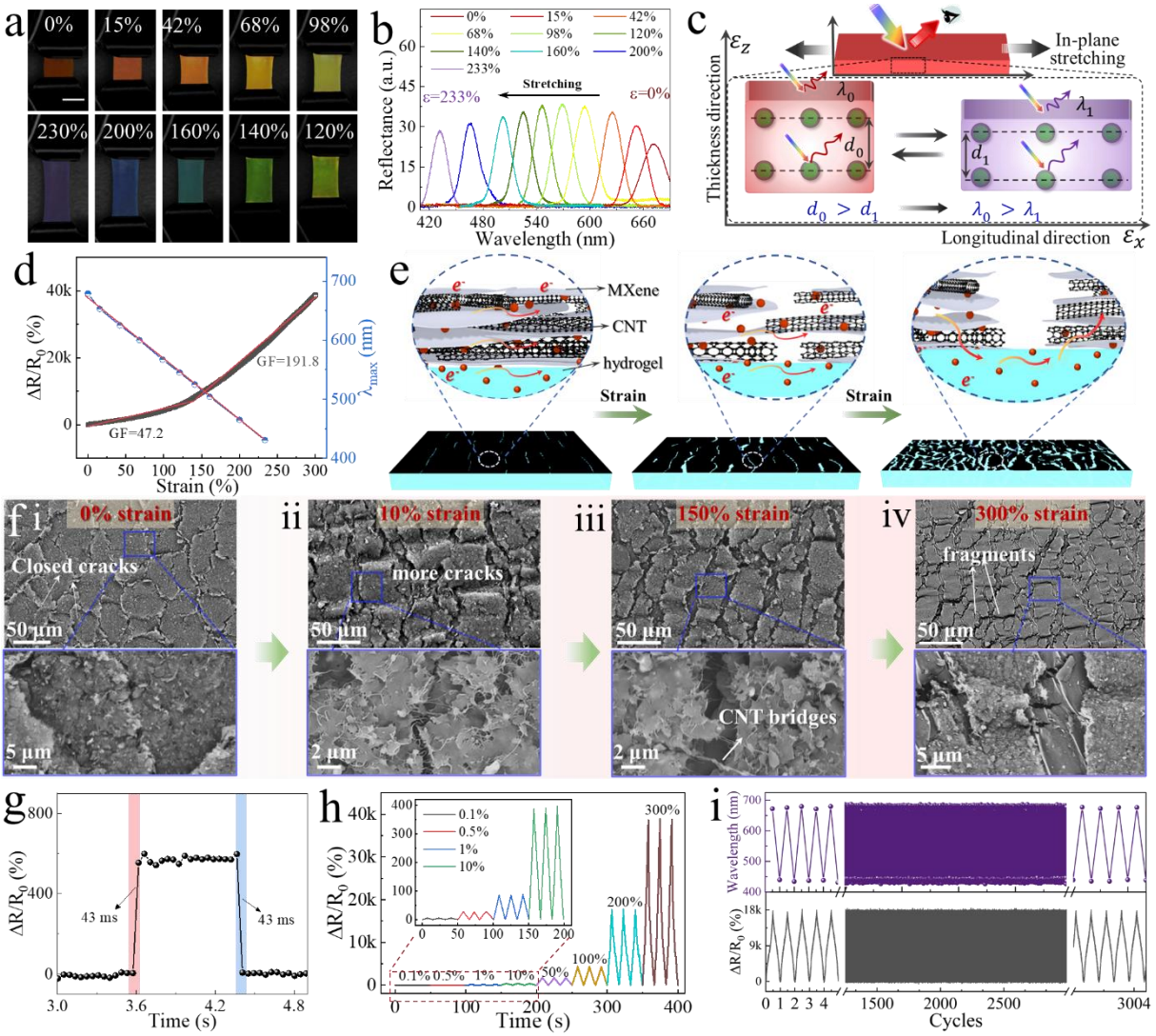

Figure 4. Optical and electrical dual-signal responses of OE-skin to tensile strain stimuli. (a) Photographs of gradual switching of structural colors under tensile strains ranging from 0 to 230%. (Scale bar = 1 cm). (b) Reflectance spectra of the dark red chromotropic film when stretched to different strains. (c) Schematic mechanism of mechanochromic response to stretching. (d) Relative resistance variations and reflectance wavelength changes at different tensile strains. (e) Schematic illustration of crack propagation in OE-skin when stretched. (f) SEM images of the cracked OE-skin taken at <i> 0%, <ii> 10%, <iii> 150%, and <iv> 300% strain. (g) Response time of resistance signals in the OE-skin at 50% strain. (h) Relative resistance variations under repeated cycles at different strains ranging from 0.1 to 300%. (i) Durability of the optical and resistance responses to 3000 loading/unloading cycles at 230%

strain.

2.4 Optical/electrical response to normal pressure

To investigate the pressure-responsive behavior of the chromotropic OE-skin, the reflected wavelengths and capacitance signals were recorded at different compressive strains by applying a pressure on a cover glass plate. Changes in structural colors at different compressive strains are shown in Figure 5a. The initially dark red color experienced a significant blue shift to orange, yellow, green, blue and violet in the stressed area as applied compressive strain increased to 60%. Their corresponding reflectance wavelength shifted from 680 to 430 nm, covering the entire visible light spectrum (Figure 5b). The pressure sensing mechanism is schematically shown in Figure 5c. Upon applying a normal pressure, the thickness of the chromotropic layer was reduced, accompanied by a decrease in the center-to-center distance of embedded photonic crystals. As a result, the wavelength of structural colors almost linearly decreased with increasing strain with a slope of 4.14 nm/% (Figure 5d). Importantly, each photonic crystal cell at the nanoscale served as a sensing unit, providing high-resolution pressure sensing without using spatially distributed, high-density sensor arrays. The green letters 'UST' clearly appeared when the OE-skin was compressed to 40% strain with convex seals which were employed to simulate the complex pressure source (Figure 5e). When a higher strain of 60% was applied, the pressure source with digital numbers '123' appeared with the blue-shifted violet structural color. The above demonstration signifies that the chromotropic OE-skin is capable of visually identifying the shape and location of complex, spatially distributed pressures.

The relative capacitance changes, $\Delta C/C_0$, were simultaneously recorded as a function of applied compressive strain using the in-built parallel-plate capacitor, as shown in Figure 5d. The pressure sensitivity, defined as $S = \delta(\Delta C/C_0)/\delta\varepsilon$, was calculated to be 21.4 at low compressive strains of 0-40% and 91.2 at high strains of 40-70%. The capacitance value of OE-skin multilayer structure depends on the dielectric constant (ϵ) of PDMS, geometric area

(A) and parallel electrode distance (d). This capacitance increased when an external pressure was applied to reduce the electrode distance, and it returned to zero without hysteresis when unloaded, as shown in Figure 5f. A short response time of 126 ms and a recovery time of 168 ms (Figure 5g) with a detection limit of 75 Pa (Figure 5h) were displayed during the pressure sensing. When the OE-skin was subjected to cycles at different maximum pressures ranging from 10 to 90 kPa, it presented a highly stable capacitive response (Figure 5i). Furthermore, Figure 5j shows the long-term durability of the dual-mode pressure sensor in terms of very consistent optical wavelength and electrical capacitance for over 5000 cycles.

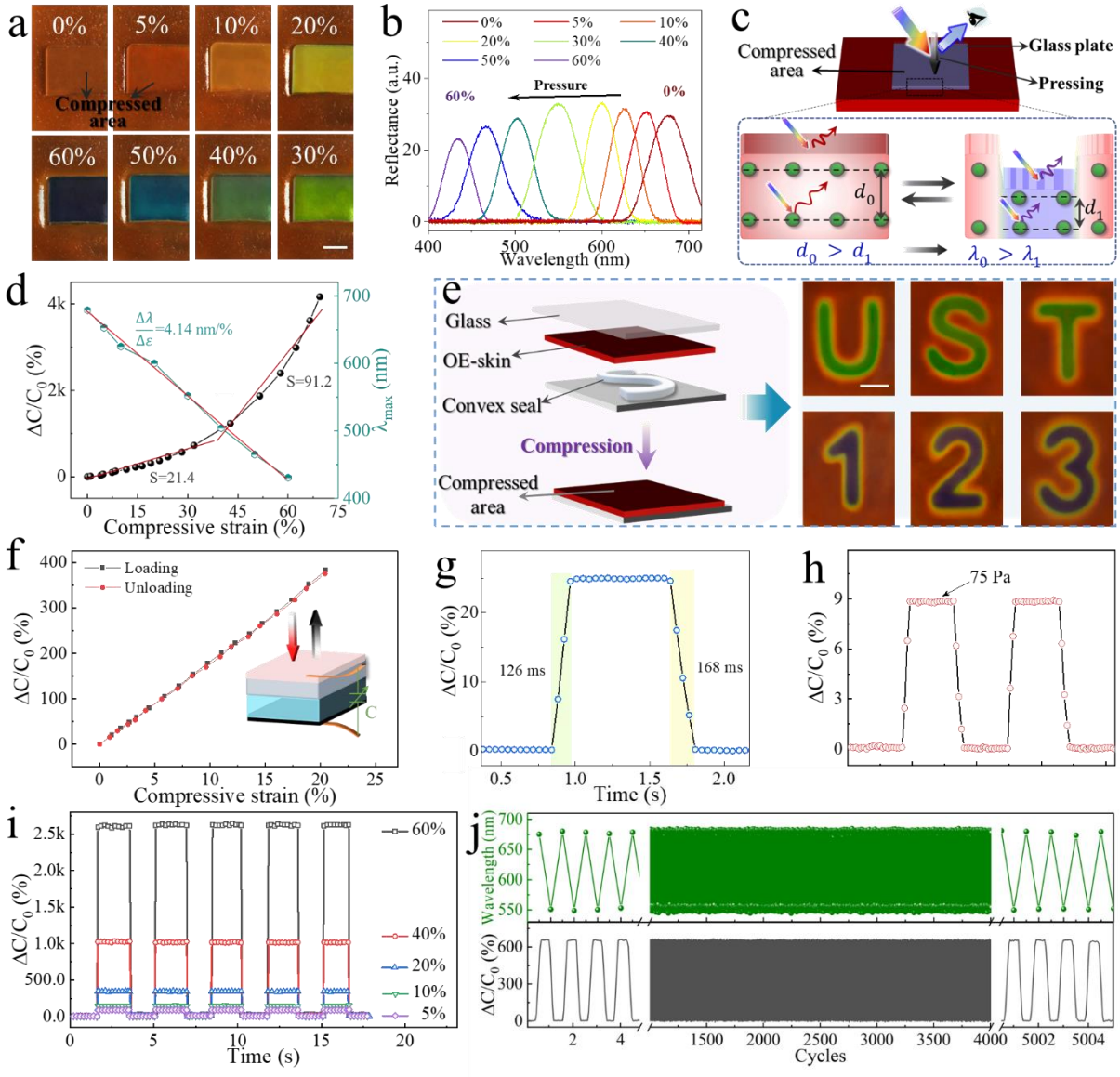

Figure 5. Optical and electrical responses of the OE-skin to normal pressure stimulus. (a)

Digital photographs showing color switching from dark red to violet (Scale bar = 1 cm), and (b) Changes in reflectance spectra from 680 nm to 430 nm when compressive strain increases from 0 to 60%. (c) Schematic mechanism of mechanochromic response to normal pressure. (d) Changes in relative capacitance and reflectance wavelengths at different compressive strains. (e) Photographs of color switching behavior induced by convex seals showing high-resolution strain distributions of the complex pressure sources. (Scale bar = 2 cm). (f) Relative capacitance response during loading and unloading. (g) Response time and (h) detection limit of the OE-skin for pressure sensing. (i) Relative capacitance variations under repeated cycles with compression ranging from 5 to 60 % strain. (j) Optical and capacitance responses to 5000 loading/unloading cycles at a pressure of 50 kPa demonstrating long-term durability of the OE-skin.

2.5 Application of the dual-signal e-skin for detecting complex deformation

Given the virtue of dual-signal sensing of both in-plane tension, in-plane compression and normal pressure, as discussed above, the OE-skin was used to further visualize complex deformation and distinguish tactile forces by integrating the optical structural color and electrical signals (Figure S21). Films with complex deformations normally involve in-plane tension and in-plane compression at different locations. In order to characterize this spatial distribution of stress, the OE-skin is specially designed with an initially green structural color, located in the visible mid-spectrum range, to perceive not only in-plane tension with blue-shifted color switching from green (560 nm) to violet (430 nm) but also in-plane compression with red-shifted color switching to dark red (680 nm), as shown in Figure S22. The potential of high-resolution stress spatial mapping of the OE-skin is demonstrated in Figure 6a. Under simple in-plane bending, the flexible film was normally subjected to tension on the convex region and compression on its concave region (Figure S23). The detailed stress or strain distribution in bending was reflected by the color pattern in the bent mechanochromic film (Figure 6a<i>), with violet structural color representing tension in the convex region, dark red

representing compression in the concave region and initial green representing the original no-stress state. This color distribution matched well with stress distributions predicted by the finite element method (FEM) simulations under the same loading condition (Figure 6a<ii>), demonstrating high spatial resolution of the OE-skin's color visualization. Meanwhile, the electrical resistance signal against the applied in-plane bending exhibited a large variation thanks to its ultrahigh strain sensitivity, while the capacitance signal for pressure sensing presented a relatively small increase representing a marginally enlarged area between parallel electrodes due to flexural stretching (Figure 6a<iii>). The torsional deformation involving more complex stress fields (Figure S24) produced elliptical in-plane compression in the center and tension at two ends, as shown by the color pattern and corresponding simulated stress distribution (Figure 6b). When the twisted film was subjected to additional stretching, the central orange color switched to yellow and light green (Figure S25), and the resistance signal experienced an enormous increase due to crack propagations in the conductive layer, as explained previously (see Figure 4e). This finding verifies that our OE-skin with a dual-signal capability allows the conversion of spatially resolved stress distribution of complex deformation into high-resolution, straightforwardly visual color maps and quantitative electrical information.

Another essential application of the OE skin is to decouple complex tactile forces based on the mechanochromism of the periodically-arranged nanoparticles. The tactile force normally involves normal pressure and additional in-plane compression and/or tension. The Fe_3O_4@C photonic crystals served as high-resolution sensing units to perceive real-time spatial profiles of the complex stress fields resulting from 3D deformation generated by tactile forces. When pressures were applied at different contact areas and loadings, the OE-skin exhibited blue-shifted color switching at contact points, allowing one to identify the pressure location and magnitude. The corresponding capacitance signal for pressure sensing increased with enlarged contact area and compressive load (Figure S26), while the resistance for in-plane strain

showed little variation, indicating a negligible in-plane tensile component. As shown in Figure 7a-c <iii>, the relative resistance or relative capacitance values were very similar for different types of tactile forces, including normal pressure (Figure 7a), shear force with normal pressure and in-plane compression components (Figure 7b) and torsion with normal pressure and in-plane torsion components (Figure 7c) with the same contact area and load. The above findings may imply that electrical signals alone cannot discriminate between the normal and shear forces due to the shortcomings of the overall resistance detection scheme in recording deformations at the small, localized regions. To detect and distinguish unknown tactile stimuli, it is necessary to integrate electrical responses with spatially distributed visual signals. Unlike the normal pressure acting alone (Figure 7a), the in-plane compression component of shear force pushed the material in the front region to bulge in the thickness direction and therefore red-shifted spectrum signals of photonic crystals (Figure 7b<ii> and Figure S27b). In addition, the immediate rear region produced marginally blue-shifted structural colors as a result of stretching, manifesting the direction of shear force. Multiple shear motions at multi-point contacts, including pinch, spread and tweak, were also successfully detected by the color switching at the contact point and adjacent region (Figure S28). For a more complex torsional motion (Figure 7c), there is a color shift from green to orange and red in the surrounding circular region, similar to under shear force, reflecting the increase in reflectance wavelength along the torsional direction indicated by the arrow (Figure 7c and Figure S27c).

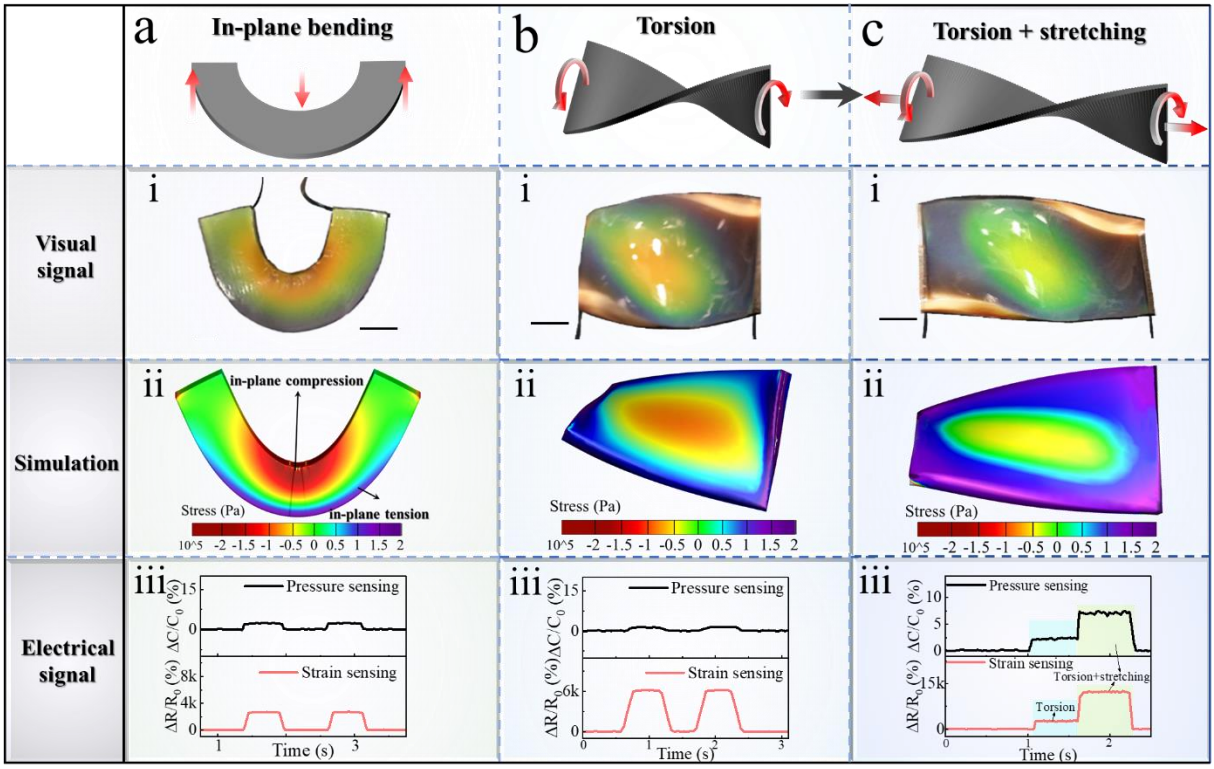

Figure 6. Demonstration of the OE-skin to visualize complex deformation. Visualization of complex deformation: structural color distributions under (a) <i> in-plane bending (scale bar = 2 cm), (b) <i> torsion and (c) <i> combined torsion and stretching. (a-c) <ii> corresponding stress distributions predicted by FEM simulations, (a-c) <iii> corresponding capacitance and resistance signals.

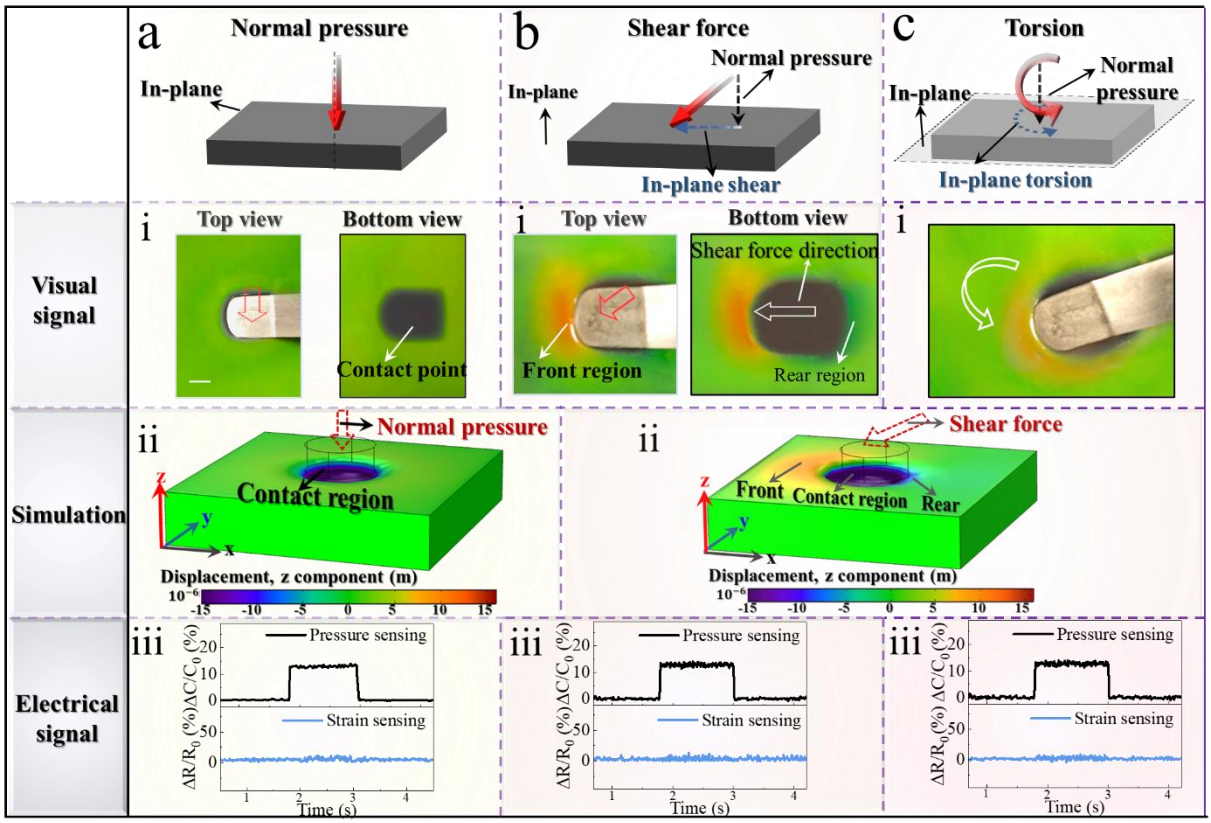

Figure 7. Demonstration of the OE-skin to discriminate different tactile forces. Structural color distributions under (a) <i> normal pressure alone, (b) <i> shear force, and (c) <i> torsion deformation, scale bar = 1 cm. (a-c) <ii> corresponding displacements in the thickness direction (z component) obtained from FEM simulations, (a-c) <iii> corresponding capacitance and resistance signals.

3. Conclusion

In summary, a highly sensitive optical and electrical dual-signal OE-skin is designed to accurately detect and interactively feedback tensile strains, normal pressures and complex tactile forces via mimicking the structural colors of chameleon and microcracked structure of spider-slit-organs. The multilayer chromotropic films consisted of a gelatin/PAM hydrogel with embedded Fe_3O_4@C particle arrays, a microcracked CNT/MXene conductive film and a parallel-plate capacitive sensor that accurately visualized various mechanical stimuli, detected tensile strains and perceived pressure stimuli, respectively. The mechanoresponsive capability derived from the non-close-packed Fe_3O_4@C photonic crystals could respond to in-plane

tensile and normal pressure with bright color-switching optical signals in the full visible spectrum from dark red (680 nm) to violet (430 nm). The crack propagation mechanism of the OE-skin enabled by the microcracked CNT/MXene conductive film delivered an ultrahigh electrical strain sensitivity with a high GF of 191.8 at a wide working range of 300% strain. The pressure sensing function of the OE-skin exhibited outstanding capacitance signals with a low detection limit of 65 Pa, a fast response speed of 126 ms and a stable operation for 5000 cycles. Through integrating the spatial distribution of optical structural colors and electrical signals of resistance and capacitance, the OE-skin was able to visualize the stress distributions of complex deformation with a high spatial-temporal resolution and quantitative electrical digitalization. Different types of tactile forces, including normal pressure, shear force combined with normal pressure and in-plane torsion, were effectively resolved by distinguishing the visual color maps between the contact points and adjacent regions. These new functional features of the OE-skin may provide a conceptually new approach in designing next-generation multifunctional sensors.

4. Experimental Section

Materials

Gelatin (300 g Bloom, Type A, from porcine skin), acrylamide (AAM, ≥ 98%), N,N'-methylene-bis-acrylamide (MBAA, 99%), photoinitiator irgacure 2959 (98%), sodium chloride (NaCl, 99%), ferrocene ($Fe(C_5H_5)_2$, ≥99%), hydrogen peroxide (H_2O_2, 30%), acetone (C_3H_6O, >98%), ethylene glycol (EG, 99%), lithium fluoride (LiF, 99.9%), and hydrochloric acid (HCl, 37%) were supplied by Sigma-Aldrich. PDMS (Sylgard 184) was supplied by Dow Corning. Titanium aluminum carbide (Ti_3AlC_2, 200 mesh) was provided by Beijing Kaifatetao Technology. Single-walled carbon nanotubes (purity ≥ 95%) were purchased from Chengdu Organic Chemical. All of the materials and chemicals were used as received without further purification.

Fabrication of Fe_3O_4@C/gelatin/PAM chromotropic layer

The superparamagnetic nanoparticles, Fe_3O_4@C, were synthesized by high temperature hydrolysis reactions. Typically, ferrocene (0.54 g) was fully dissolved in acetone (54 mL). After mechanical stirring for 20 min and sonication for 5 min, different amounts of H_2O_2 (1.1-2.0 mL) were slowly added to control the size of synthesized nanoparticles, ranging from 130 to 250 nm. Subsequently, the obtained mixture solution was sealed in a l00 ml polyphenylene-lined stainless-steel autoclave and heated at 230 ℃ for 70 h. After the reaction, the prepared nanoparticles were cooled to room temperature overnight, repeatedly washed with acetone and finally collected with a magnet. In the following step, 0.1g of dried Fe_3O_4@C was dispersed in the mixture of 4 mL EG and 6 mL deionized (DI) water. Then, 1g of gelatin, 1g of AAM, 2.86 mg of MBAA (0.286 wt% relative to AAM) and 0.42 mg irgacure 2959 (0.042 wt% relative to AAM) were added to the solution to prepare gelatin/AAM at 10%/10% mass ratio. For comparison of mechanical properties, gelatin/AAM powders with different mass ratios and concentrations were dissolved by mechanically stirring at 1000 rpm and 90 ℃ for 1 h. The homogenous solutions were placed above a cuboid magnet (of dimensions 50 mm × 50 mm × 20 mm) to obtain nanoparticle arrays with different structural colors. The photonic crystal structures in the gel precursor were fixed by freezing at -20 ℃ for 5 h and then crosslinked by UV light (365 nm) at 4 ℃ for 1 h to obtain the Fe_3O_4@C/gelatin/PAM chromotropic layer.

Fabrication of OE-skin

The conductive CNT/MXene hybrid film was prepared by mixing the exfoliated MXene nanosheets and dispersed CNTs. 0.5 g Ti_3AlC_2 powders were added into the mixture of 0.8 g LiF and 10 mL HCl (9 M) in a Teflon beaker. The Al layer of the Ti_3AlC_2 phase was selectively etched by stirring at 500 rpm and 35 ℃ for 24 h. The products were centrifuged at 3500 rpm for 10 min and washed with DI water several times to remove impurities until the pH of the supernatant increased to 6-7. The dried sediment after centrifugation (0.2 g) was re-

dispersed in 50 mL DI water by gentle sonication for 10 min and stirring at 500 rpm and room temperature for 1 h to obtain a homogeneous, exfoliated MXene dispersion (4 mg/mL). Meanwhile, 50 mg CNTs powders were dispersed in 100 mL DI water by adding 1 g Triton X-100 after stirring at 1000 rpm for 30 min and probe sonication (Sonic VCX 750) at 400 W for 30 min, achieving a concentration of 0.5 mg/mL. Desired amounts of MXene solution were added into the CNT solution to obtain varying mass ratios of CNT/MXene ranging from 0 to 100% after stirring at 1000 rpm for 2 h. The hybrid filler dispersion was infiltrated under vacuum to obtain CNT/MXene hybrid films with different thicknesses on a cellulose membrane (pore size 0.45 μm, N8645-100EA, SIGMA). The dried CNT/MXene film was attached to the chromotropic layer. Subsequently, a thin PDMS film of 50 μm in thickness was attached to the other side of the chromotropic layer by crosslinking the mixture of base and curing agent at a ratio of 15:1 to serve as the dielectric layer. An electrode layer containing 10% AAM, 40% EG, 1M NaCl, 0.0286 wt% MBAA and 0.0042 wt% irgacure 2959 was dip-coated on top of the PDMS dielectric layer which was photopolymerized under the UV light (365 nm) for 30 min. Finally, the whole assemble was encapsulated with PDMS to avoid water evaporation from the hydrogel.

Characterization and measurements of sensing performance

The SEM (JSM-7100) was used to examine the morphologies of the photonic crystal arrays, and the microcracks of CNT/MXene conductive film. The inner structure of the magnetic nanoparticles was examined by TEM (JEOL 2010). The diameters of the prepared nanoparticles were measured on a particle size analyzer (Mastersizer 3000). The functional groups of gelatin, PAM and Fe_3O_4@C/gelatin/PAM hydrogels were analyzed by FT-IR (Bruker Vertex 70 Hyperion 1000). The transmittance of gelatin, gelatin/PAM and PDMS films was evaluated by UV/Vis spectroscopy (Perkin Elmer Lambda 20). The chemical structure and surface morphology of MXene flakes were characterized by XPS (PHI5600, Physical Electronics) and AFM (NanoScope, Dimension 3100). The magnetic hysteresis

curves of Fe_3O_4@C particles were recorded by vibrating on a magnetometer (LakeShore 9300). The mechanical properties, including tensile and compressive strengths, of gelatin/PAM hydrogels with different concentrations were measured on a universal testing machine (UTM-12) equipped with digital multimeters. The adhesion strength of the gelatin/PAM hydrogels were assessed using the lap-shear tests. Rectangular hydrogels of 25 mm in length and 15 mm in width were placed between two substrates made of metal, plastic, glass, pig skin or PDMS sheets and the test samples were pressed gently to ensure good contacts. The tensile strain-stress curves were recorded by stretching the substrates at a cross-head speed of 15 mm/min at room temperature. The adhesion strength was calculated by dividing the maximum load with the initial attached area. Three samples of each group were tested and the average values were recorded. For the electrical resistance and capacitance signals, the conductive carbon tapes attached to the ends of the CNT/MXene conductive film and the PAM ionic hydrogel film were connected to a digital multimeter (891 LCR meter) with a voltage of 1 V and a sweep frequency of 1 kHz. The conductivity of the CNT/MXene film was measured using a four-point probe method (Ecopia HMS-5500). The structural colors at different tensile and compressive strains were recorded with a digital camera and the corresponding reflection wavelengths were acquired by a fiber-optic spectrometer (USB 2000, Ocean Optics) at a fixed glancing angle. The stress distribution fields under complex deformation and various tactile conditions were numerically calculated using the FEM (Table S2) with COMSOL Multiphysics software.

Supporting Information

Supporting Information is available from the Wiley Online Library or the author.

Acknowledgements

This project was financially supported by the Research Grants Council (GRF Projects: 16205517, 16209917 and 16200720) and the Innovation and Technology Commission

(ITS/012/19) of Hong Kong SAR. Technical assistance from the Materials Characterization and Preparation Facilities (MCPF) and the Advanced Engineering Material Facility (AEMF) at HKUST are appreciated.

Received: ((will be filled in by the editorial staff))

Revised: ((will be filled in by the editorial staff))

Published online: ((will be filled in by the editorial staff))

References

[1] I. You, D. G. Mackanic, N. Matsuhisa, J. Kang, J. Kwon, L. Beker, J. Mun, W. Suh, T. Y. Kim, J. B. H. Tok, Z. Bao, U. Jeong, *Science* **2020**, 370, 961.
[2] H. Kim, J. Choi, K. K. Kim, P. Won, S. Hong, S. H. Ko, *Nat Commun* **2021**, 12, 4658.
[3] Y. Yu, J. Nassar, C. Xu, J. Min, Y. Yang, A. Dai, R. Doshi, A. Huang, Y. Song, R. Gehlhar, A. D. Ames, W. Gao, *Sci Robot* **2020**, 5, aaz7946.
[4] H. Chen, Y. Jing, J. H. Lee, D. Liu, J. Kim, S. Chen, K. Huang, X. Shen, Q. B. Zheng, J. Yang, S. Jeon, J. K. Kim, *Mater. Horiz.* **2020**, 7, 2378.
[5] H. Zhang, D. Liu, J. H. Lee, H. M. Chen, E. Kim, X. Shen, Q. B. Zheng, J. Yang, J. K. Kim, *Nano-Micro Lett* **2021**, 13, 122.
[6] J. H. Lee, H. M. Chen, E. Kim, H. Zhang, K. Wu, H. M. Zhang, X. Shen, Q. B. Zheng, J. Yang, S. Jeon, J. K. Kim, *Mater. Horiz.* **2021**, 8, 1488.
[7] Q. F. Shi, Z. X. Zhang, Y. Q. Yang, X. C. Shan, B. Salam, C. K. Lee, *ACS Nano* **2021**, 15, 18312.
[8] J. H. Lee, E. Kim, H. Zhang, H. Chen, H. Venkatesan, K. Y. Chan, J. Yang, X. Shen, J. Yang, S. Jeon, J. K. Kim, *Adv. Funct. Mater.* **2022**, 32, 2107570.
[9] A. Chortos, J. Liu, Z. Bao, *Nat. Mater.* **2016**, 15, 937.
[10] X. L. Ma, C. F. Wang, R. L. Wei, J. Q. He, J. Li, X. H. Liu, F. C. Huang, S. P. Ge, J. Tao, Z. Q. Yuan, P. Chen, D. F. Peng, C. F. Pan, *ACS Nano* **2022**, 16, 2789.
[11] D. Jung, C. Lim, H. J. Shim, Y. Kim, C. Park, J. Jung, S. I. Han, S. H. Sunwoo, K. W. Cho, G. D. Cha, D. C. Kim, J. H. Koo, J. H. Kim, T. Hyeon, D. H. Kim, *Science* **2021**, 373, 1022.
[12] J. H. Zhang, H. M. Yao, J. Y. Mo, S. Y. Chen, Y. Xie, S. L. Ma, R. Chen, T. Luo, W. S. Ling, L. F. Qin, Z. K. Wang, W. Zhou, *Nat Commun* **2022**, 13, 5076.
[13] X. C. Qu, Z. Liu, P. C. Tan, C. Wang, Y. Liu, H. Q. Feng, D. Luo, Z. Li, Z. L. Wang, *Sci. Adv.* **2022**, 8, eabq2521.
[14] F. F. Li, R. Wang, C. Y. Song, M. M. Zhao, H. H. Ren, S. S. Wang, K. Liang, D. W. Li, X. H. Ma, B. W. Zhu, H. Wang, Y. Hao, *ACS Nano* **2021**, 15, 16422.
[15] Q. B. Zheng, J. H. Lee, X. Shen, X. Chen, J. K. Kim, *Mater. Today* **2020**, 36, 158.
[16] H. C. Wan, Y. Q. Cao, L. W. Lo, J. Y. Zhao, N. Sepulveda, C. Wang, *ACS Nano* **2020**, 14, 10402.
[17] K. C. Xu, Y. Y. Lu, K. Takei, *Adv. Funct. Mater.* **2021**, 31, 2007436.
[18] L. Cai, H. Wang, Y. Yu, F. Bian, Y. Wang, K. Shi, F. Ye, Y. Zhao, *Natl Sci Rev* **2019**, 7, 644.
[19] D. Zhang, J. Wang, Z. Tong, H. Ji, H. Y. Qu, *Adv. Funct. Mater.* **2021**, 31, 2106577.
[20] J. Xu, C. Ban, F. Xiu, Z. Tian, W. Jiang, M. Zhang, H. Zhang, Z. Zhou, J. Liu, W. Huang, *ACS Appl. Mater. Interfaces* **2021**, 13, 30205.

[21] Y. Zhuang, R. J. Xie, *Adv. Mater.* **2021**, 33, 2005925.
[22] X. Wang, M. Que, M. Chen, X. Han, X. Li, C. Pan, Z. L. Wang, *Adv. Mater.* **2017**, 29, 1605817.
[23] G. Kim, S. Cho, K. Chang, W. S. Kim, H. Kang, S. P. Ryu, J. Myoung, J. Park, C. Park, W. Shim, *Adv. Mater.* **2017**, 29, 1606120.
[24] H. Eoh, Y. Jung, C. Park, C. E. Lee, T. H. Park, H. S. Kang, S. Jeon, D. Y. Ryu, J. Huh, C. Park, *Adv. Funct. Mater.* **2022**, 32, 2103697.
[25] L. Su, Z. Jiang, Z. Tian, H. Wang, H. Wang, Y. Zi, *Nano Energy* **2021**, 79, 105431.
[26] H. H. Chou, A. Nguyen, A. Chortos, J. W. F. To, C. Lu, J. Mei, T. Kurosawa, W. G. Bae, J. B. H. Tok, Z. Bao, *Nat Commun* **2015**, 6, 8011.
[27] G. Q. Lin, M. Q. Si, L. G. Wang, S. X. Wei, W. Lu, H. Liu, Y. Zhang, D. Y. Li, T. Chen, *Adv Opt Mater* **2022**, 10, 2102306.
[28] W. L. Qiu, C. G. Zhang, G. Q. Chen, H. Zhu, Q. Zhang, S. P. Zhu, *ACS Appl. Mater. Interfaces* **2021**, 13, 26490.
[29] D. K. Kwon, J. M. Myoung, *ACS Nano* **2020**, 14, 8716.
[30] Y. X. Dong, A. Bazrafshan, A. Pokutta, F. Sulejmani, W. Sun, J. D. Combs, K. C. Clarke, K. Salaita, *ACS Nano* **2019**, 13, 9918.
[31] Y. Zhao, W. C. Gao, K. Dai, S. Wang, Z. Q. Yuan, J. N. Li, W. Zhai, G. Q. Zheng, C. F. Pan, C. T. Liu, C. Y. Shen, *Adv. Mater.* **2021**, 33, 2102332.
[32] J. I. Lee, H. Choi, S. H. Kong, S. Park, D. Park, J. S. Kim, S. H. Kwon, J. Kim, S. H. Choi, S. G. Lee, D. H. Kim, M. S. Kang, *Adv. Mater.* **2021**, 33, 2100321.
[33] W. F. Yang, W. Gong, W. Gu, Z. X. Liu, C. Y. Hou, Y. G. Li, Q. H. Zhang, H. Z. Wang, *Adv. Mater.* **2021**, 33, 2104681.
[34] S. Wei, H. Qiu, H. Shi, W. Lu, H. Liu, H. Yan, D. Zhang, J. Zhang, P. Theato, Y. Wei, T. Chen, *ACS Nano* **2021**, 15, 10415.
[35] I. Jurewicz, A. A. K. King, R. Shanker, M. J. Large, R. J. Smith, R. Maspero, S. P. Ogilvie, J. Scheerder, J. Han, C. Backes, J. M. Razal, M. Florescu, J. L. Keddie, J. N. Coleman, A. B. Dalton, *Adv. Funct. Mater.* **2020**, 30, 2002473.
[36] Y. Wang, W. Niu, C. Y. Lo, Y. Zhao, X. He, G. Zhang, S. Wu, B. Ju, S. Zhang, *Adv. Funct. Mater.* **2020**, 30, 2000356.
[37] W. Niu, X. Cao, Y. Wang, B. Yao, Y. Zhao, J. Cheng, S. Wu, S. Zhang, X. He, *Adv. Funct. Mater.* **2021**, 31, 2009017.
[38] H. Zhang, H. Chen, J. H. Lee, E. Kim, K. Y. Chan, H. Venkatesan, M. H. Adegun, O. G. Agbabiaka, X. Shen, Q. Zheng, J. Yang, J. K. Kim, *Adv. Funct. Mater.* 2022, 2208362.
[39] W. Yang, S. Yamamoto, K. Sueyoshi, T. Inadomi, R. Kato, N. Miyamoto, *Angew. Chem. Int. Ed.* **2021**, 60, 8466.
[40] F. Fu, Z. Chen, Z. Zhao, H. Wang, L. Shang, Z. Gu, Y. Zhao, *PNAS* **2017**, 114, 5900.
[41] H. Wang, Y. Liu, Z. Chen, L. Sun, Y. Zhao, *Sci. Adv.* **2020**, 6, eaay1438.
[42] L. Bai, Y. Jin, X. Shang, L. J. Shi, H. Y. Jin, R. Zhou, S. Q. Lai, *Chem. Eng. J.* **2022**, 438, 135596.
[43] Q. Q. Lyu, S. Z. Wang, B. L. Peng, X. D. Chen, S. Du, M. M. Li, L. B. Zhang, J. T. Zhu, *Small* **2021**, 17, 2103271.
[44] L. Bai, Y. Jin, X. Shang, H. Y. Jin, Y. T. Zhou, L. J. Shi, *J Mater Chem A* **2021**, 9, 23916.
[45] Z. Y. Chen, Y. R. Yu, J. H. Guo, L. Y. Sun, Y. J. Zhao, *Adv. Funct. Mater.* **2021**, 31, 2007527.
[46] Y. Wang, L. Shang, G. Chen, L. Sun, X. Zhang, Y. Zhao, *Sci. Adv.* **2020**, 6, eaax8258.
[47] Q. Zhou, J. G. Park, J. Bae, D. Ha, J. Park, K. Song, T. Kim, *Adv. Mater.* **2020**, 32, 2001467.
[48] H. Zhang, J. Guo, Y. Wang, L. Sun, Y. Zhao, *Adv. Sci.* **2021**, 8, 2102156.

[49] Y. P. Wang, X. F. Cao, J. Cheng, B. W. Yao, Y. S. Zhao, S. L. Wu, B. Z. Ju, S. F. Zhang, X. M. He, W. B. Niu, *ACS Nano* **2021**, 15, 3509.
[50] K. Zhao, X. Cao, Y. Alsaid, J. Cheng, Y. Wang, Y. Zhao, X. He, S. Zhang, W. Niu, *Chem. Eng. J.* **2021**, 426, 130870.
[51] Z. Y. Shi, L. X. Meng, X. L. Shi, H. P. Li, J. Z. Zhang, Q. Q. Sun, X. Y. Liu, J. Z. Chen, S. R. Liu, *Nano-Micro Lett* **2022**, 14, 141.
[52] H. Tan, Q. Lyu, Z. Xie, M. Li, K. Wang, K. Wang, B. Xiong, L. Zhang, J. Zhu, *Adv. Mater.* **2019**, 31, 1805496.
[53] X. Shi, Z. Deng, P. Zhang, Y. Wang, G. Zhou, L. T. de Haan, *Adv. Funct. Mater.* **2021**, 31, 2104641.
[54] Y. Wang, Y. Yu, J. Guo, Z. Zhang, X. Zhang, Y. Zhao, *Adv. Funct. Mater.* **2020**, 30, 2000151.
[55] D. Kang, P. V. Pikhitsa, Y. W. Choi, C. Lee, S. S. Shin, L. Piao, B. Park, K. Y. Suh, T. I. Kim, M. Choi, *Nature* **2014**, 516, 222.
[56] Y. Sun, Y. Wang, Y. Liu, S. Wu, S. Zhang, W. Niu, *Adv. Funct. Mater.* **2022**, 32, 2204467.
[57] X. Q. Wang, C. F. Wang, Z. F. Zhou, S. Chen, *Adv Opt Mater* **2014**, 2, 652.

TOC

Bioinspired by the structural color of chameleons and microcracked structure of spider-slit-organs, a highly sensitive optical/electrical skin (OE-skin) is designed to detect external mechanical stimuli by means of simultaneous electrical signals and vividly visible color-switching responses. The integrated dual-signal OE-skin enables one to visualize stress distributions arising from complex deformation in a quick and accurate manner.

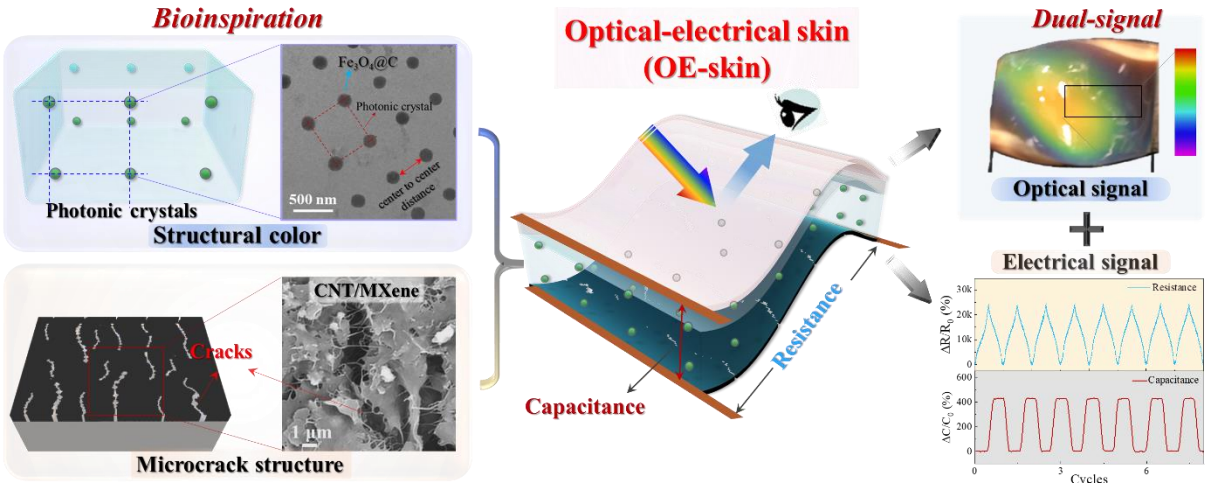

Supporting information

Mechanochromic optical/electrical skin for ultrasensitive dual-signal sensing

Heng Zhang[1], Haomin Chen[1], Jeng-Hun Lee[1], Eunyoung Kim[1], Kit-Ying Chan[1,2], Harun Venkatesan[1], Xi Shen[1,2]*, Jinglei Yang[1,3]*, and Jang-Kyo Kim[1,4]*

H. Zhang, H. Chen, J.H. Lee, E. Kim, Prof. X. Shen, Prof. Q.B. Zheng, Prof. J.L. Yang, Prof. J.K. Kim
[1] Department of Mechanical and Aerospace Engineering, The Hong Kong University of Science and Technology, Clear Water Bay, Kowloon, Hong Kong 999077, China.
[2] Department of Aeronautical and Aviation Engineering, The Hong Kong Polytechnic University, Hung Hom, Kowloon, Hong Kong 999077, China.
[3] HKUST Shenzhen-Hong Kong Collaborative Innovation Research Institute, Futian, Shenzhen 518048, China.
[4] School of Mechanical and Manufacturing Engineering, University of New South Wales, Sydney, NSW 2052, Australia.
E-mail: xi.shen@polyu.edu.hk (X. Shen); maeyang@ust.hk (J.L. Yang); mejkkim@ust.hk (J.K. Kim)

Keywords: interactive sensing, structural color, mechanochromism, stretchable electronics, dual-signal.

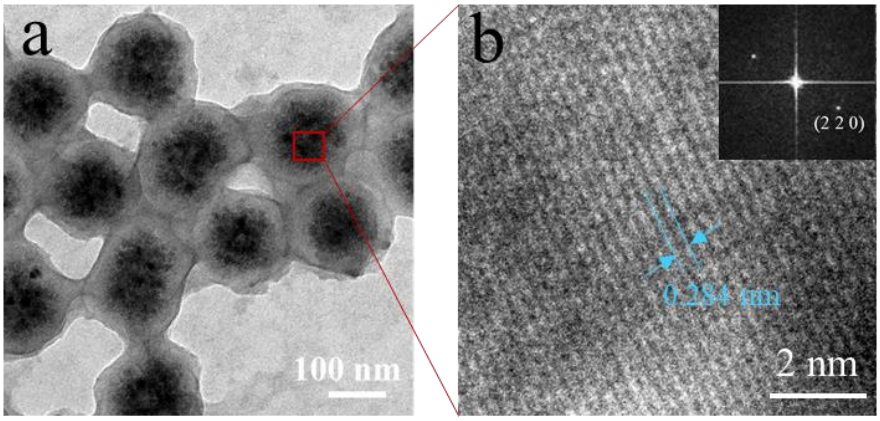

Figure S1. (a) TEM image of Fe_3O_4@C nanoparticles showing the core-shell structure. (b) High-resolution TEM image of primary magnetite crystallite with fast Fourier transform (FFT) of Fe_3O_4 in inset.

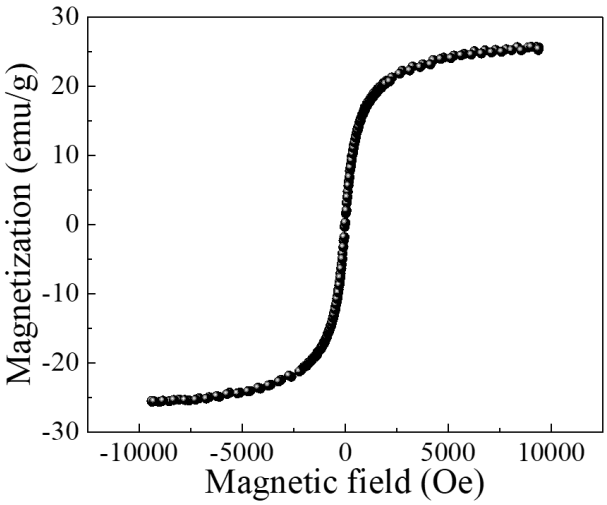

Figure S2. Magnetic hysteresis curve of Fe_3O_4@C nanoparticles at room temperature between -10 and 10 kOe.

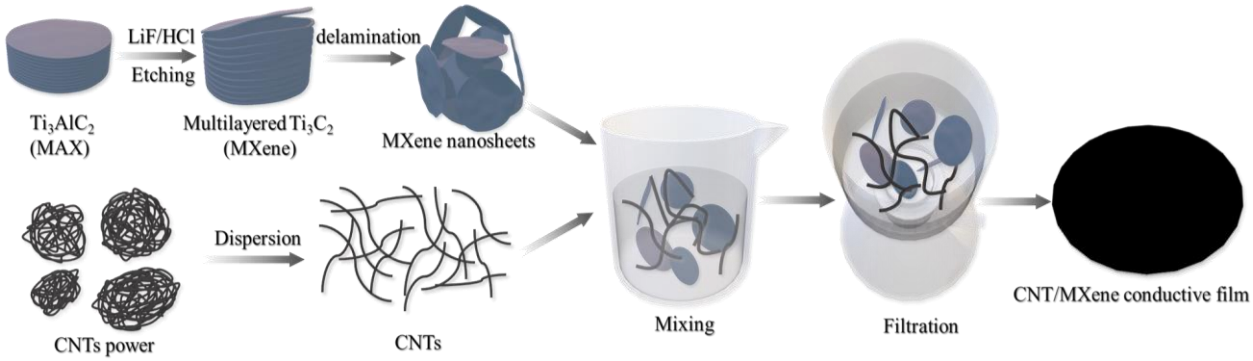

Figure S3. Fabrication process of the CNT/MXene conductive film.

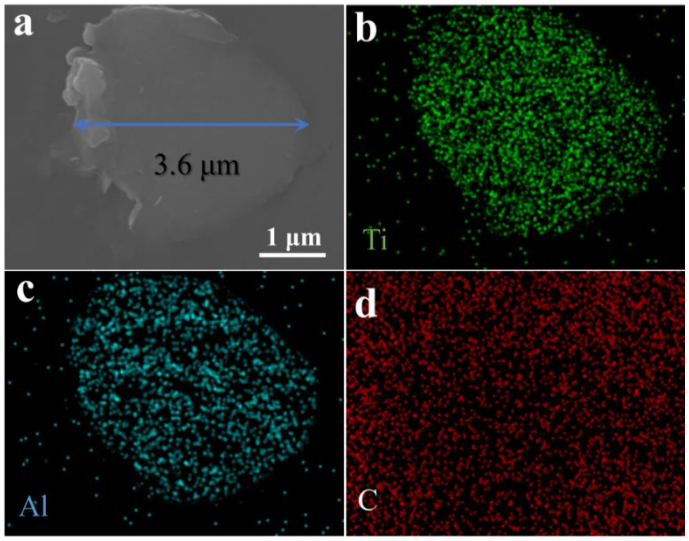

Figure S4. SEM image of MXene nanosheet (a) and the corresponding element maps of elements (b) Ti, (c) Al and (d) C.

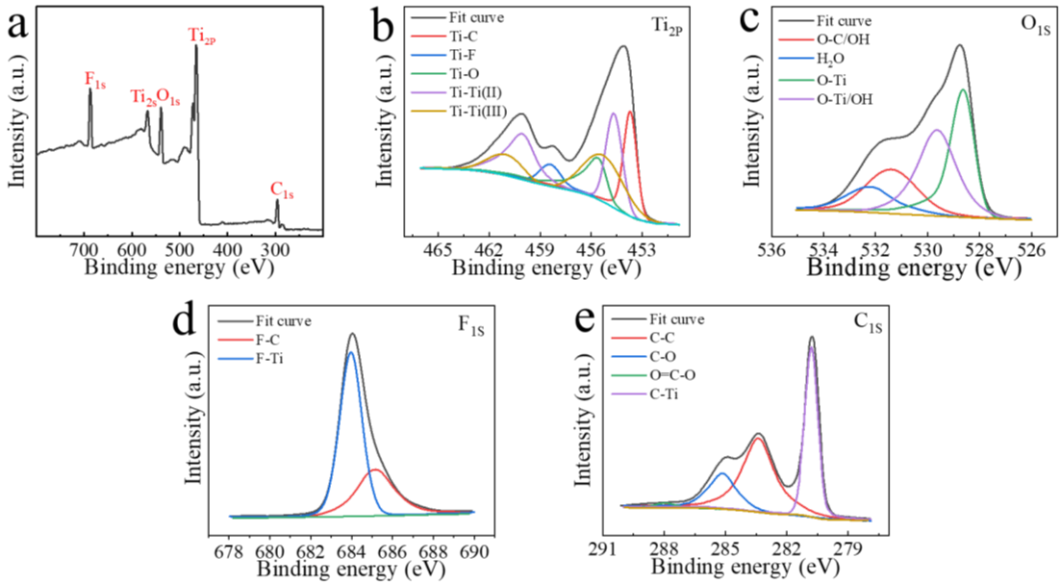

Figure S5. (a) XPS spectra of MXene nanosheets and high resolution XPS spectra of (b) Ti, (c) O, (d) F, and I C.

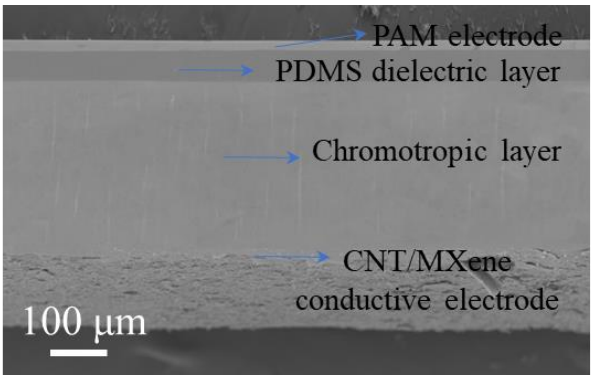

Figure S6. Cross-sectional SEM image of the OE-skin showing the multilayer structure.

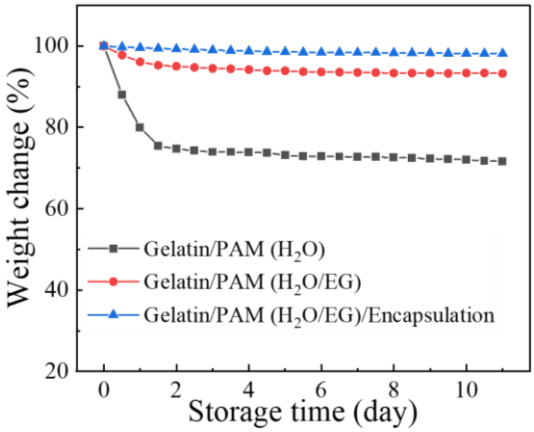

Figure S7. Weight changes of gelatin/PAM hydrogel prepared with water solvent, gelatin/PAM with water/EG solvent and gelatin/PVA with water/EG solvent and PDMS

encapsulation. The gelatin/PAM hydrogel with water/EG solvent encapsulation shows no weight reduction, testament to excellent long-term stability.

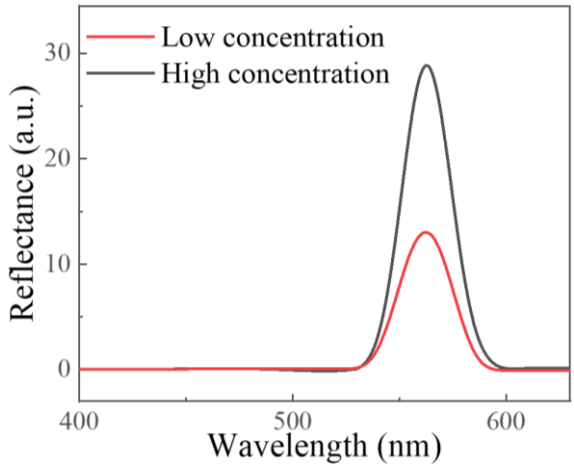

Figure S8. Reflectance spectra of the chromotropic films prepared with low and high Fe_3O_4@C concentrations.

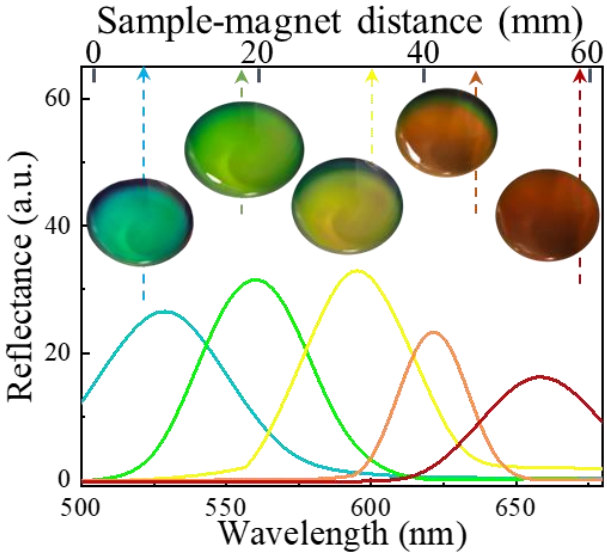

Figure S9. Reflectance spectra of the Fe_3O_4@C/gelatin/PAM solutions in the beaker above the magnet with different sample-magnet distances.

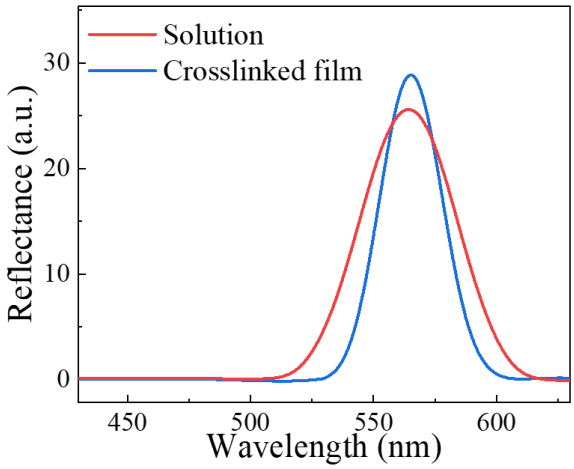

Figure S10. Reflectance spectra of the chromotropic film before and after polymerization.

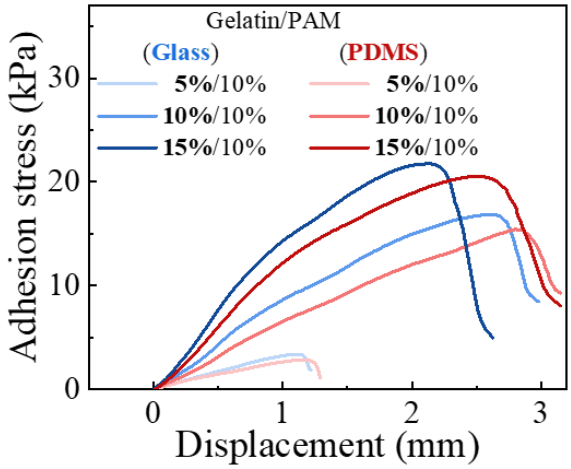

Figure S11. Adhesion stress with glass and PDMS substrates vs displacement curves of the gelatin/PAM hydrogels prepared with different gelatin concentrations.

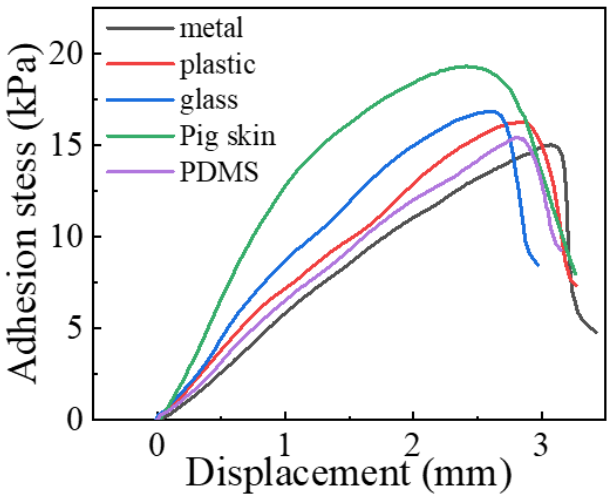

Figure S12. Adhesion stress vs displacement curves of the gelatin/PAM hydrogels with different substrates.

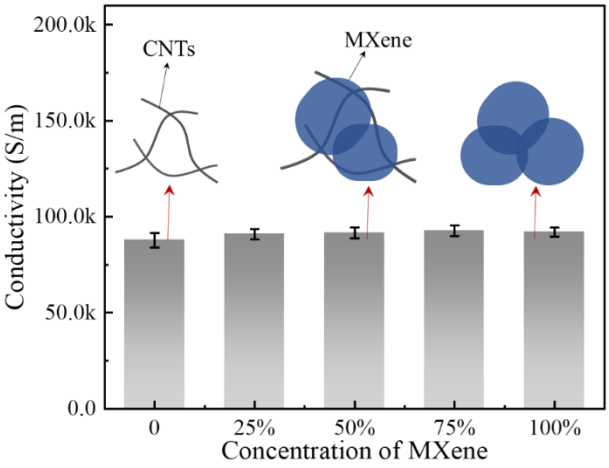

Figure S13. High electrical conductivity of the CNT/MXene films prepared with different MXene concentrations.

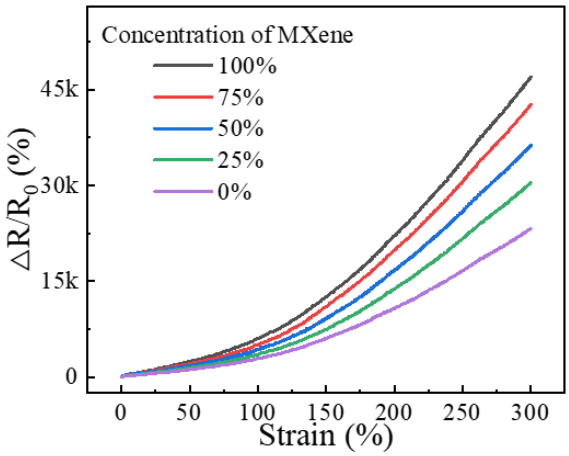

Figure S14. Relative resistance variations vs strain of the CNT/MXene conductive films prepared with different MXene concentrations.

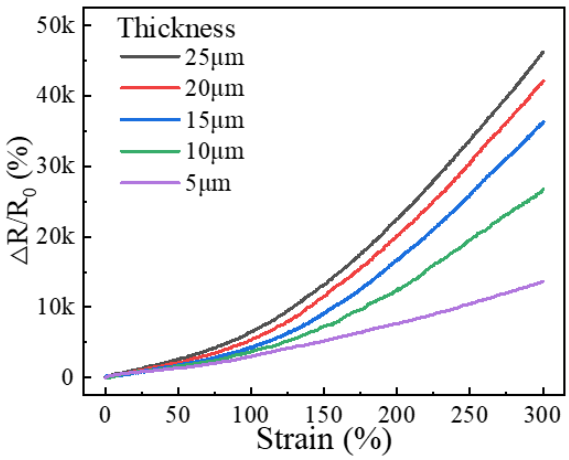

Figure S15. Relative resistance variations vs strain curves of the CNT/MXene films with different thicknesses.

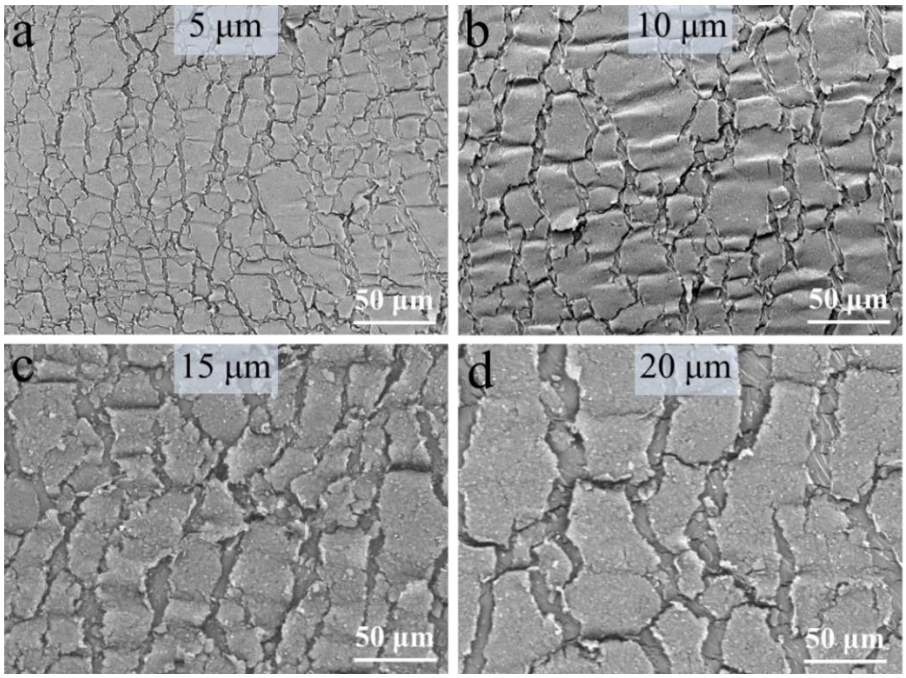

Figure S16. SEM images of the CNT/MXene conductive films with different thicknesses showing microcracks when they are subjected to 150% tensile strain.

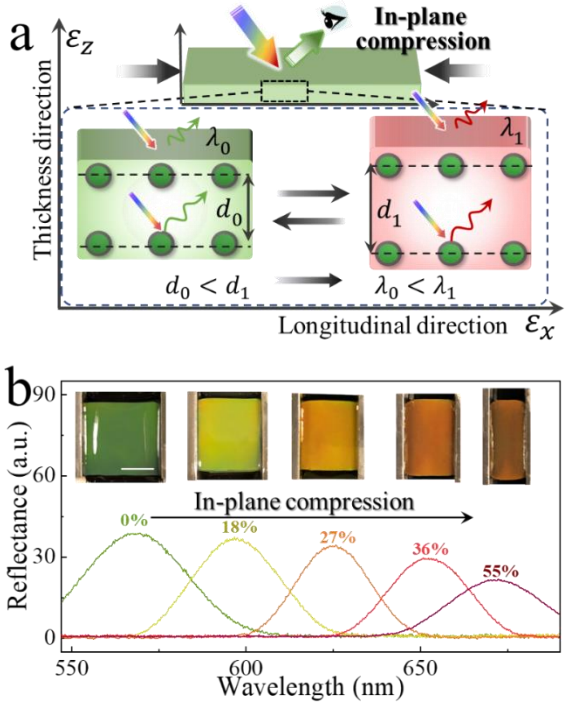

Figure S17. (a) Illustration of mechanochromic mechanisms under in-plane compression. (b) Changes in reflectance spectra and the corresponding structural colors of the chromotropic film with initially green color under different in-plane compressive strains. (Scale bar = 5 mm).

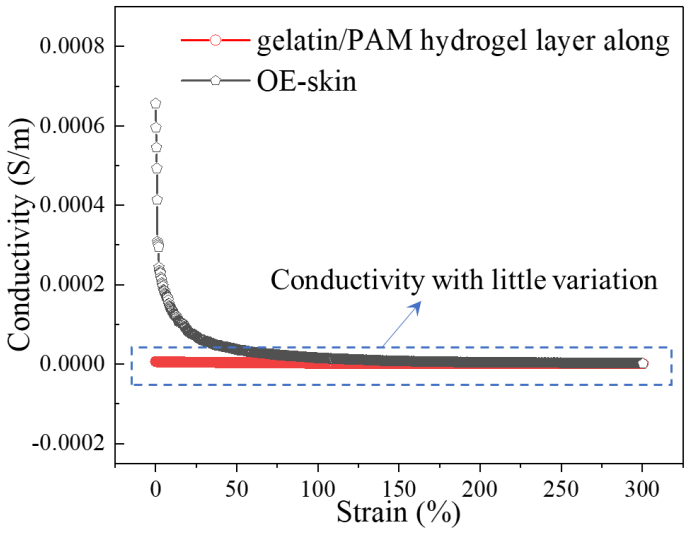

Figure S18. Conductivity variation vs strain curves of the gelatin/PAM hydrogel layer and assembled OE-skin.

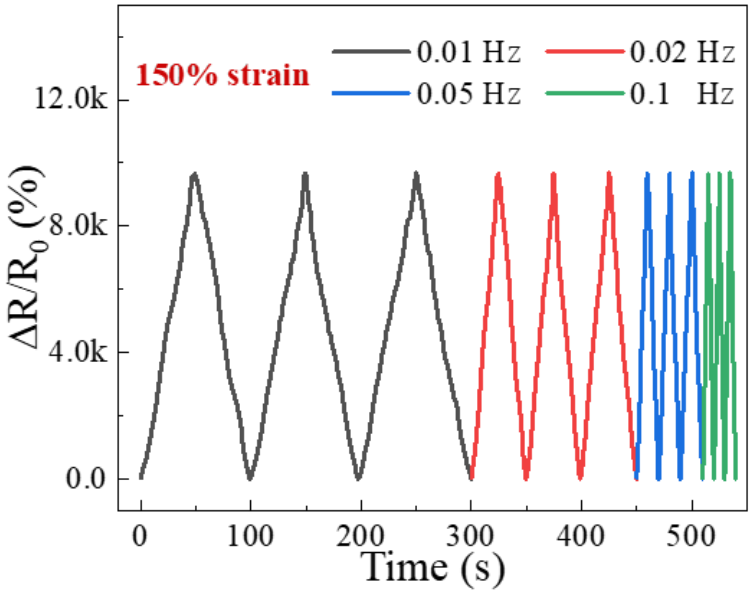

Figure S19. Stable relative resistance variation measured at 150% strain and different stretching frequencies.

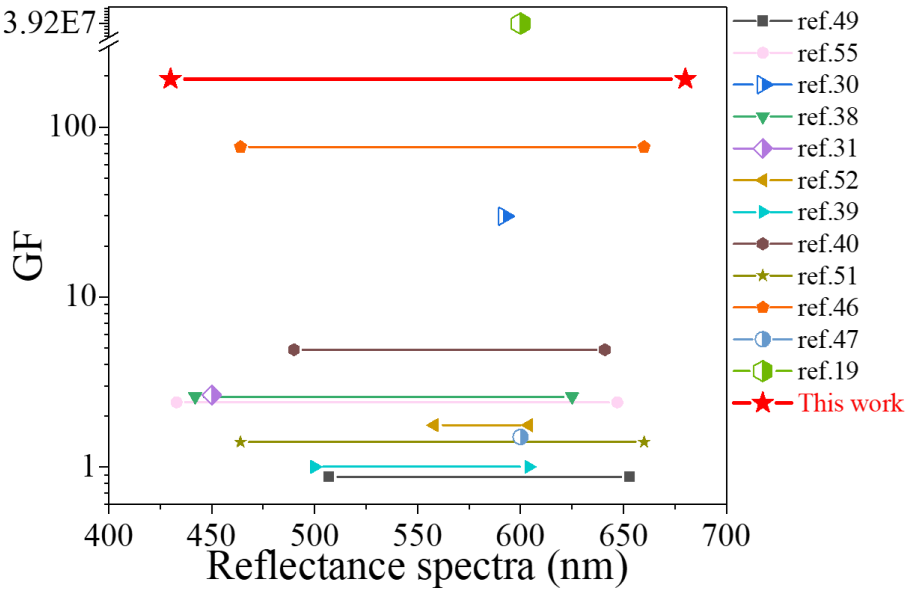

Figure S20. Comparison of GF and shifted reflectance spectra of visual signals between the current OE-skin and existing state-of-the-art sensors with dual-signal capabilities.

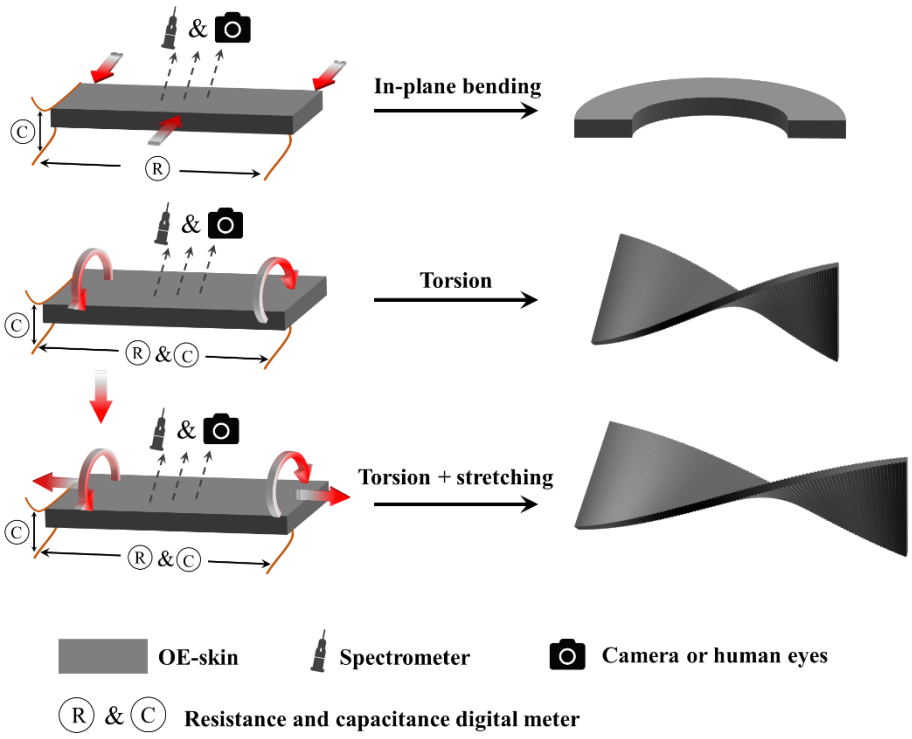

Figure S21. Schematic diagrams of in-plane bending, torsion and torsion + stretching tests.

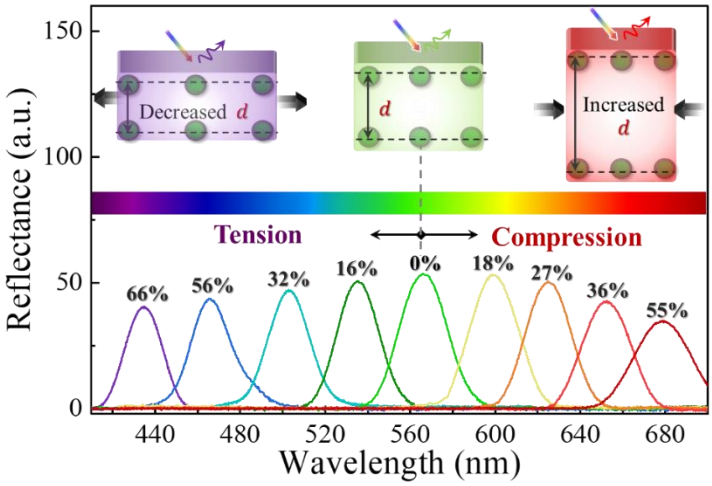

Figure S22. Illustration of mechanochromic mechanisms under in-plane tension and compression, and the corresponding reflectance spectra of the initially green OE-skin.

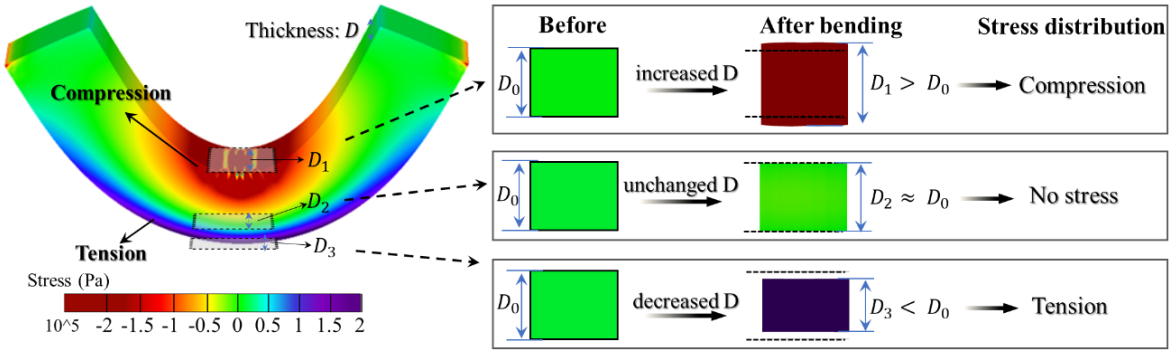

Figure S23. Stress distribution (left) and thickness variations (right) at different locations of OE-skin under in-plane bending.

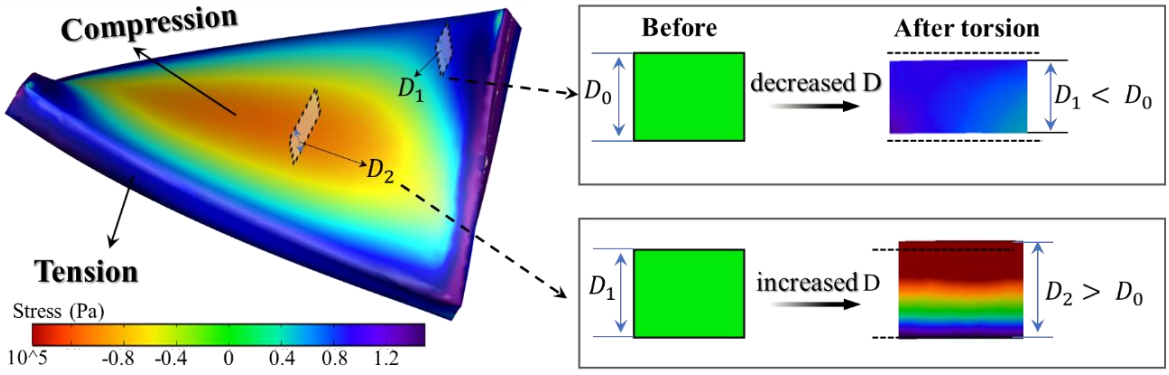

Figure S24. Stress distribution (left) and thickness variations (right) at different locations of OE-skin under torsional deformation.

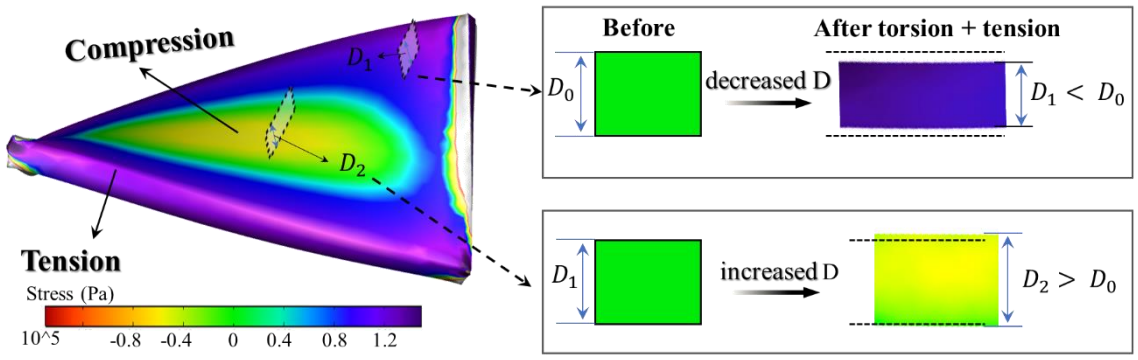

Figure S25. Stress distribution and thickness variations at different locations of OE-skin under torsion + stretching.

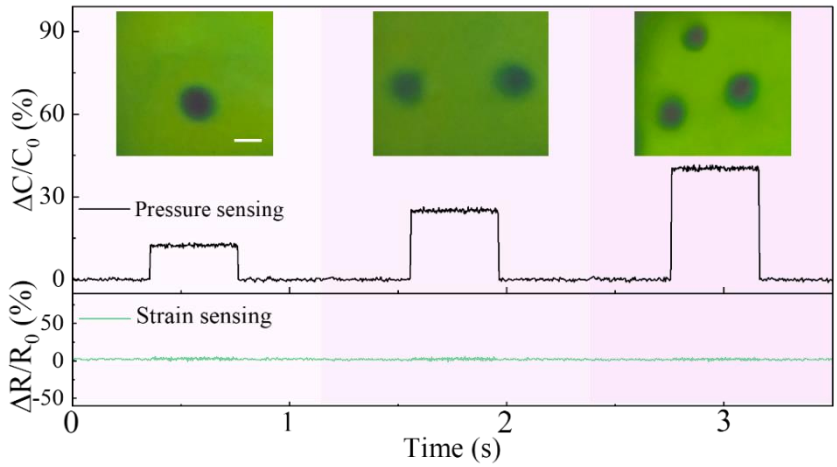

Figure S26. Relative capacitance and resistance responses to the normal pressures on different contact areas. Photographs of corresponding structural color distribution in inset showing the locations of pressure sources. Scale bar = 1 cm.

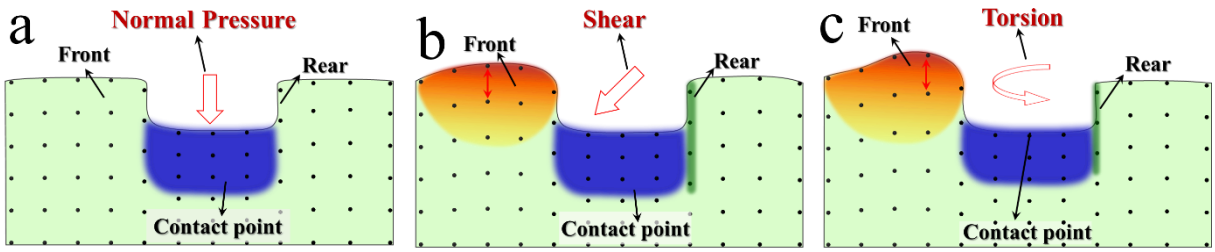

Figure S27. Illustration of displacements in the thickness direction of OE-skin under (a) normal pressure, (b) shear force and (c) torsion.

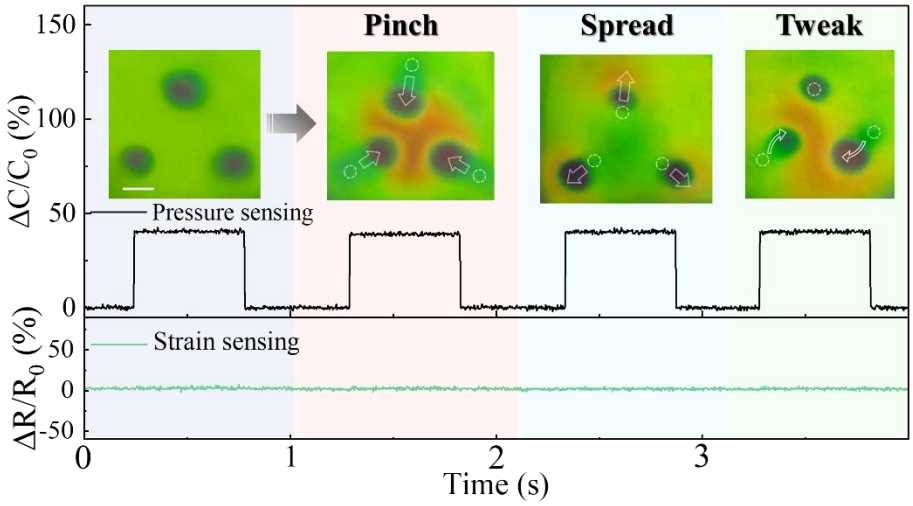

Figure S28. Capacitance and resistance responses to multiple shear motions including pinch, spread and tweak. Photographs of corresponding structural color distributions in inset. Scale bar = 1 cm.

Table S1. Comparison of in-plane strain and pressure sensing performance between our OE-skin and existing state-of-the-art dual-signal sensors.

Functional material		**Matrix**	**Mechanism**	**Range of reflectance wavelength**	**Sensing range**	**Sensitivity**	**Ref**
Optical	**Electrical**						
Inverse opal scaffold of SiO_2	PEDOT: PSS and GO	Polyacrylamide, silk fibroin	Structural color	Red to blue-green (653 nm - 507 nm)	0-400% (strain)	0.875 (strain)	[48]
Inverse opal structure of SiO_2	CNTs	Polyurethane and polydopamine	Structural color	Red to blue (647 nm - 433 nm)	0-100% (strain)	2.4 (strain)	[54]
Red fluorescent RB-PHEAA	CNTs film with microcracks	PDMS	mechanofluorensce	FL intensity at 592 nm (0 - 30 a. u.)	0-100% (strain)	29.9 (strain)	[27]
Inverse opal structure of SiO_2	free ions (Br^- and Na^+)	Poly(acrylic acid-co-sodium	Structural color	Red to blue (625 nm - 442 nm)	0-120% (strain), 0-40 kPa	2.59 (strain), 3.73	[42]

		acrylate)/polydopamine (PACSD)			(pressure)	kPa^{-1} (pressure)	
Spiropyran (SP)	free ions (Cl^- and Na^+)	PAM and polymethyl acrylate	Mechanochromism	Blue color intensity (0.22-0.04)	0-100% (strain)	2.65 (strain)	[28]
PS@SiO_2 photonic arrays	conductive polyester textile	PTMG-IPDI-PDO supramolecular elastomer	Mechanochromism	Red to green (604 nm-558 nm)	0-200% (strain)	1.76 (strain)	[50]
non-close-packed array of SiO_2	Ionic liquid of [EMIm][TFSI]	poly(ethylene glycol) phenyl ether acrylate (PEGPEA)	Structural color	Yellow to blue (604 nm-500 nm)	0-55% (strain)	1 (strain)	[43]
liquid-crystal structure of hydroxypropyl cellulose	free ions (Al^{3-} and Zn^{2+})	poly(2-amino-4-pentenoic acid sodium-co-acrylamide) (PASCA)	Structural color	Red to green for strain sensing (641nm- 490 nm), Red to blue for pressure sensing (641 nm-450 nm)	0-67% (strain), 0-25 kPa	4.9 (strain), 3.14 kPa^{-1} (pressure)	[44]
N,N-dimethyl-1-dodecylamine N-oxide (C_{12}DMAO)	free ions (Cl^- and Na^+)	poly(diacetone acrylamide-co-acrylamide) (PDAAM-co-PAAM)	Structural color	Red to blue (660 nm-464 nm)	0-100% (strain) 0-50% (pressure)	1.4 (strain)	[49]
poly(dodecylglyceryl itaconate) (PDGI)	CNTs	PAM and Ecoflex silicone elastomer	Structural color	Red to blue (660 nm-464 nm)	0-200% (strain)	76.5 (strain)	[36]
Tris(2,2′-bipyridine)r	an ionic liquid of	polyurethane	electrochemiluminescen	ECL (yellow) intensity of	0-100% (strain),	1.5 (strain)	[32]

uthenium(II) hexafluorophosphate ([Ru(bpy)3][PF6]2)			ce	2.15-3.33 a.u. (strain), intensity of 1-10.8 a.u. (pressure)	0-60 kPa (pressure)		
Organic security fluorescent agent	CNT/MXene with microcracks	polyurethane	Mechanoluminescent effect	Light intensity of yellow color (0-11 a.u.)	0-65% (strain)	3.92×10^7 (strain)	[31]
Mechanoluminescent agent of ZnS: Cu^{2+} phosphor	ferroelectric P(VDF-TrFE) nanofibers	SEBS thermoplastic elastomer	mechanoluminescent-triboelectric synergistic effect	Light intensity of yellow color (30-120 a.u.)	0-200% (strain)	487 V/% (strain)	[33]
Non-close-packed array of magnetic Fe_3O_4@C	CNT/MXene film with microcracks	Gelatin/PAM	Structure color and crack propagation mechanism	Red to violet (680 nm-430 nm)	0-230% (strain), 0-60% (pressure)	191.9 (strain), 21.4 %/% (pressure)	**This work**

Table S2. Parameters setting for FEM simulation calculation in COMSOL.

Parameter	Value
Density	1100 kg/m^3
Poisson's ratio	0.3
Material model of hydrogel	Mooney-Rivlin
Compressibility	Nearly incompressible material
Model parameters	$C_{10} = 0.37\ MPa$; $C_{01} = 0.11\ MPa$.
Bulk modulus	$1 \times 10^4\ MPa$